Available online at www.sciencedirect.com
SCIENCE DIRECT®
Journal of Computational Physics 194 (2004) 1–34
JOURNAL OF COMPUTATIONAL PHYSICS
www.elsevier.com/locate/jcp

An implicit Vlasov–Fokker–Planck code to model non-local electron transport in 2-D with magnetic fields

R.J. Kingham *, A.R. Bell

Blackett Lab., Plasma Physics Group, Imperial College, London SW7 2AZ, UK

Received 25 November 2002; received in revised form 19 August 2003; accepted 20 August 2003

Abstract

We describe an implicit finite-difference scheme for solving the Vlasov–Fokker–Planck equation and Maxwell's equations in 2 spatial dimensions including, for the first time, self-consistent magnetic fields. These equations model the coupled phenomena of magnetic field generation and magnetised electron transport in collisional plasmas, such as laser-produced plasmas, in the non-relativistic limit. The kinetic description of the plasma enables the scheme to properly describe these phenomena in the regime where the temperature and density scale lengths become comparable to the transport mean-free-path. In addition to including the self-consistent magnetic field, other improvements over previous Fokker–Planck codes have been made which result in a robust scheme that can work with a large time step. The scheme employs Cartesian geometry and solves for the electromagnetic field components E_x, E_y and B_z. Extension to all field components and cylindrical geometry is possible.

Keywords: Finite difference scheme; Implicit; Sparse matrix; Fokker–Planck; Vlasov; Magnetic field; Maxwell's equations; Plasma; Electron transport; Non-local

1. Introduction

Energy transport [1,2] is an important process in plasma physics which impacts on many areas including, laser–plasmas, astrophysical plasmas, magnetic confinement fusion and Z-pinches. Magnetic field generation in plasmas [3–5] is another important phenomenon that is particularly relevant to laser–plasmas and astrophysical plasmas. This paper concerns modelling of these processes in the area of laser–plasma interactions, particularly in the contexts of the interaction of intense, short laser pulses with solid targets [6] and inertial fusion energy [7] (which uses laser or particle beams to compress and heat plasma to achieve fusion). Intense laser–solid interaction looks like a promising source of high energy, low emittance proton

* Corresponding author. Tel.: +44-0-207-5947637; fax: +44-0-207-5947658.
E-mail address: rj.kingham@ic.ac.uk (R.J. Kingham).

0021-9991/$ - see front matter © 2003 Elsevier B.V. All rights reserved.
doi:10.1016/j.jcp.2003.08.017

and ion beams, as well as high energy photons and neutrons [6]. Successful development of inertial fusion energy (IFE) power generation schemes and laser–plasma-based sources of energetic particles requires a proper understanding of energy transport including the effect of magnetic fields. To do this, the electron Vlasov–Fokker–Planck equation and Maxwell's equations need to be solved. Strong magnetic fields can severely affect energy transport [1] while heating plasma can result in the production of magnetic field [5,8]. For example, non-parallel electron density and temperature (or pressure) gradients act as a source of *B*-fields [4]; $\partial_t \mathbf{B} \propto -\nabla n_e \times \nabla T_e$. In IFE this source can generate magnetic fields reaching $\sim$1 MG [9] which is strong enough to inhibit thermal transport. As mentioned above energy transport and magnetic field generation are relevant elsewhere in plasma physics. For instance, the same *B*-field generation mechanism (as above) is also considered to be a candidate for the 10^{-21}–10^{-17} G strength primordial, cosmic, seed *B*-field that has subsequently been amplified (by a dynamo mechanism) to produce the μG strength magnetic field observed in galaxies [10]. In this context, it is known as the Biermann battery [3]. Therefore, the scheme described here may be relevant to other areas of plasma physics too.

Formulation of a model that can properly and accurately describe electron transport and magnetic field generation under realistic laser–plasma conditions is a challenging task. This stems from the need to self-consistently treat electrons with a range of collisionalities. Because the mean-free-path of an individual electron scales as $\lambda_{mfp} \propto v^4$ the motion of slow electrons is dominated by collisions. Conversely, fast electrons are collisionless so that their motion is governed by electric fields which decelerate them and magnetic fields which deflect their trajectories into curved orbits with a radius of curvature of $r_g = m_e v/eB$. Crucially, the fields that deflect the fast, collisionless electrons are strongly affected by collisions [11,12]. A return current of cold, collisional electrons $\mathbf{j}_c$ must be drawn to approximately balance the current of fast electrons $\mathbf{j}_f$ with $\nabla \cdot \mathbf{j}_c = -\nabla \cdot \mathbf{j}_f$ so that quasineutrality is maintained. It is the resistivity α of the cold electrons that determines the electric field $\mathbf{E} \approx \alpha \mathbf{j}_c$ and the degree to which the currents balance that determines the magnetic field, $\nabla \times \mathbf{B} = \mu_o(\mathbf{j}_c + \mathbf{j}_f)$. When there are a significant number of energetic electrons possessing long mean-free-paths that exceed the characteristic lengths L_T and L_n over which the plasma temperature and density vary the plasma becomes *non-local* because its evolution at a given point depends intimately on the condition of plasma far away. Previously the Vlasov–Fokker–Planck (VFP) equation has been solved numerically ignoring magnetic fields in 1-D (1 spatial dimension) [13,14] and 2-D [15,16] to address heat-flow down steep temperature gradients in unmagnetised plasma. Under these conditions the classical, fluid description of transport [1,2], which makes the local approximation, breaks down. They found that non-local effects are responsible for thermal transport inhibition [13] and reduced lateral thermal smoothing [15]. A 1-D code has previously been written to solve the VFP and Maxwell's equations including magnetic fields [17], but it cannot describe magnetic field generation by thermal sources or how *B*-fields affect heating uniformity being 1-dimensional.

Until now, there has not been a fully kinetic 2-D model of electron transport with magnetic fields and *B*-field generation that adequately treats the whole range of electron collisionality present under realistic conditions. Previous 2-D models that include *B*-fields have fallen into three categories; (1) fluid codes, (2) PIC or Vlasov codes, and (3) hybrid codes. Fluid codes [9,18–20] cannot describe non-local effects because they utilise classical, transport theory, e.g. [1]. Strictly they are only valid for highly collisional plasmas where $\bar{\lambda} \ll L_n, L_T$, where the $\bar{\lambda}$ is the *average* electron collisional mean-free-path and $L_n = n/|\nabla n|$, $L_T = T/|\nabla T|$. Particle-in-cell (PIC) codes [21,22] and Vlasov codes [23] are fully kinetic and are ideally suited to collisionless plasmas. Typically PIC codes tend to use explicit methods and consequently require a time step small enough to resolve the fastest frequency present in the problem. They also suffer from the so called 'finite grid instability' [22] whereby the plasma numerically heats up until the electron debye length is resolved by the grid. These limitations mean that multidimensional, explicit, PIC cannot readily simulate the low temperature, high density plasma created in laser–solid interactions. PIC codes utilising implicit methods do exist [24]. Implicitness greatly relaxes the time step constraint and mitigates the effects of the finite grid instability, so that lower temperatures and higher densities can be dealt with. One spatial

dimension PIC codes with electron–ion collisions have successfully been applied to fast electron transport through solid density plasma [12]. Two spatial dimension PIC codes with electron collisions also exist, both explicit [25] and implicit [26]. Explicit 2-D PIC is unable to access conditions where collisions dominate for the bulk of the electrons, though. Even though implicit methods overcome this particular problem, the PIC method in general struggles to adequately resolve the distribution function in a given cell when a realistic sized, 2-D problem is addressed. Statistical noise and under resolution of the electron distribution lead to an inaccurate treatment of collisions and can overwhelm real physical effects present. Hybrid models [27–30] have emerged which could be considered a cross between PIC and fluid codes. They treat high energy electrons kinetically while the bulk of the electrons which make up the background through which the energetic particles travel are simply described as a resistive fixed medium or fluid. They have been used to investigate resistive inhibition of hot electron penetration through 'gold foam' (electron density of $n_e = 1.3 \times 10^{21}$ cm^{-3}) in 1-D [27] and the propagation of laser-generated energetic electrons beams through tens of microns of solid density plasma due to magnetic collimation in 2-D [29]. Enhanced fluid models with separate fluids for hot and cold electrons [31,32] or a convolution treatment of transport fluxes (without magnetic fields) [33] exist which provide a partial description of non-local transport. But neither hybrid codes nor enhanced fluid models are fully kinetic. We note that many numerical schemes also exist [34–37] which solve the Fokker–Planck equation alone without the Vlasov equation or Maxwell's equations and only consider the velocity dimensions of phase space. While these schemes accurately and efficiently describe relaxation and thermalisation of particles in a spatially uniform system, they are not able to model transport (or B-field generation) since they ignore all spatial dimensions and the electric field.

Here, we described the first 2-D VFP code to self-consistently include magnetic fields. Consequently this code has the unique capability of being able to model magnetic field generation and electron transport in the presence of magnetic fields, fully kinetically and with an accurate treatment of collisions. It can therefore access experimentally relevant regimes where existing models and codes are not valid or not well suited. The code is called IMPACT which stands for 'Implicit Magnetised Plasma and Collisional Transport'. As well as being the first 2-D VFP code to self-consistently include magnetic fields IMPACT incorporates several other innovations. First, it treats the electric field implicitly as well as the electron distribution function unlike previous VFP codes [13–17] which overcomes problems in maintaining quasineutrality [16]. Second, it is the first 2-D VFP code to solve the full matrix equation that arises when using implicit differencing. The benefit of this fully implicit approach is that it makes the code robust and able to use large time steps well exceeding the characteristic collision time. The third innovation is retention of electron inertia which can greatly reduce the computational effort needed to solve the implicit matrix equation (see Section 5) as well as keeping physical effects which are normally discarded.

In comparison to other laser–plasma numerical schemes IMPACT is particularly suited to describing non-local effects arising from collisional, thermal transport in the presence of steep temperature and density gradients and magnetic fields. It also provides a good, non-local description of magnetized transport in the non-relativistic background of electrons in the uniform, solid-density plasma scenario. In both situations it is adept at modelling magnetic field generation by collisional and semi-collisional mechanisms. Like previous 2-D VFP codes it currently uses the diffusive approximation (see Section 2.1) which limits its ability to deal with strong anisotropy in the electron distribution. Therefore other methods are better suited to modelling laser-absorption by collective, collisionless processes (i.e., PIC) and transport of highly, collimated, beams of relativistic electrons through dense, uniform plasma background (i.e., hybrid codes).

The rest of this paper proceeds as follows. In Section 2 the equations to be solved numerically are given and explained. Section 3 covers the numerical scheme. Results from and descriptions of tests carried out to verify the code are presented in Section 4. The implication of the test results, general observations about the code and routes for improving it are discussed in Section 5. Finally, conclusions are given in Section 6.

2. The model and equations

In this section, we describe the system that is modelled, give the equations that need to be solved, state the approximations used and discuss some important physical features and phenomena contained in the model.

The goal is to calculate how the energy absorbed into a plasma from a short, intense, laser pulse is transported away from the laser focus by the heated electrons in 2-D Cartesian geometry. The generation of magnetic fields that is driven by the flow of energy away from the hot spot and the subsequent feedback of these *B*-fields on the electron transport are also to be taken into account self-consistently. We assume the plasma is stationary, the ions are cold (i.e., $v_{\mathrm{ti}} \ll v_{\mathrm{te}}$, where v_{ti} and v_{te} are the ion and electron thermal speeds, respectively) and neglect hydrodynamic motion since we are interested in strong laser heating over timescales short compared with either the hydro timescale or the thermalisation time between electrons and ions. We also assume that the ionisation state of the plasma into which the absorption takes place does not change in time, e.g., a fully ionised plasma. Though the ion density $n_{\mathrm{i}}(x,y)$ and $Z(x,y)$ are time independent, they need not be uniform so that density ramps and different materials can be modelled.

In order to properly model transport of absorbed energy away from the laser focus under intense heating (where $\overline{\lambda} \ll L_T, L_n$ is *not* valid) the full range of electron collisionality needs to be taken into account. We therefore consider the electron Vlasov–Fokker–Planck equation

$$\left[\frac{\partial}{\partial t} + \mathbf{v}\cdot\nabla_r - \frac{e}{m_{\mathrm{e}}}(\mathbf{E}+\mathbf{v}\times\mathbf{B})\cdot\nabla_v\right] f(\mathbf{v},\mathbf{r},t) = -\nabla_v\cdot\{f(\mathbf{v},\mathbf{r},t)\langle\Delta\mathbf{v}\rangle\} + \tfrac{1}{2}\nabla_v\nabla_v : \{f(\mathbf{v},\mathbf{r},t)\langle\Delta\mathbf{v}\Delta\mathbf{v}\rangle\} \quad (1)$$

together with Ampère's and Faraday's laws for a description of the magnetic field

$$\nabla\times\mathbf{B} = \mu_o\mathbf{j}, \quad (2)$$

$$\nabla\times\mathbf{E} = -\frac{\partial\mathbf{B}}{\partial t}. \quad (3)$$

The left-hand side of (1) is the Vlasov equation which on its own would describe the collisionless evolution of $f(\mathbf{v},\mathbf{r},t)$ the electron, one-particle distribution function in the presence of the macroscopic electric and magnetic fields $\mathbf{E}$ and $\mathbf{B}$ and spatial gradients in the electron density, temperature, pressure, etc. The effect of both electron–electron (*e–e*) and electron–ion (*e–i*) collisions on the evolution of f is represented by the Fokker–Planck collision operator on the right-hand side. $\langle\Delta\mathbf{v}\rangle$ is the average velocity deflection due to multiple, simultaneous, small angle Coulomb collisions for an ensemble of electrons moving with velocity $\mathbf{v}$ and is known as the coefficient of dynamical friction. Similarly $\langle\Delta\mathbf{v}\Delta\mathbf{v}\rangle$ is known as the coefficient of dynamical diffusion since it describes how collisions tend to spread out the range of velocities of an ensemble of electrons initially all moving at velocity $\mathbf{v}$. Both $\langle\Delta\mathbf{v}\rangle$ and $\langle\Delta\mathbf{v}\Delta\mathbf{v}\rangle$ vary with position $\mathbf{r}$ and time t. The reason for neglecting the displacement current $(1/c^2)\partial\mathbf{E}/\partial t$ (where c is the speed of light in vacuum) on the right-hand side of Eq. (2) will be explained below.

2.1. Cartesian tensor expansion

Rather than directly dealing with the full distribution $f(v_x,v_y,v_z,x,y,t)$ we use a reduced velocity description

$$f(\mathbf{v},x,y,t) \sim f_0(v,x,y,t) + \mathbf{f}_1(v,x,y,t)\cdot\hat{\mathbf{v}}. \quad (4)$$

This is known as the *diffusion approximation*. This approach reduces the phase space for the distribution from five dimensions (that is three velocity dimensions v_x, v_y, v_z and two configuration space dimensions x, y)

to three dimensions ($|\mathbf{v}|, x, y$) but splits the distribution into three parts f_0, f_x, and f_y. We take $f_z = 0$ here (see Section 2.3). This reduction enables solution of the Vlasov–Fokker–Planck via a finite difference (FD) scheme. The FD approach permits a more accurate treatment of collisions than would be afforded by a particle-based scheme, the other main method of solving Eq. (1), which would be prone to statistical noise and would struggle to adequately resolve the distribution. Classical transport theory makes the local approximation whereby f_0 the isotropic part of the distribution is assumed to be Maxwellian and has the form $f_M = n_e/(2\pi k_B T_e/m_e)^{3/2} \exp(-m_e v^2/2k_B T_e)$. Setting $f_0 = f_M$ reduces the Vlasov–Fokker–Planck equation to the well-known electron fluid equations for mass and energy continuity plus equations for mass flux (momentum) and energy flux (heat flow). The momentum equation is often referred to as the generalised Ohm's law. No such restriction is made here so the kinetic equations for the evolution of the reduced distribution (Eq. (10) and (11) below) must be solved. Eq. (4) is obtained by decomposing the distribution function into a Cartesian tensor series in velocity [38]

$$f(\mathbf{v},\mathbf{r},t) = \sum_p f_p(v,\mathbf{r},t) :_p (\hat{\mathbf{v}})^p = +f_0(v,\mathbf{r},t) + \mathbf{f}_1(v,\mathbf{r},t)\cdot\hat{\mathbf{v}} + \mathbf{f}_2(v,\mathbf{r},t) : \hat{\mathbf{v}}\hat{\mathbf{v}} + \cdots \tag{5}$$

retaining only the leading 2 terms. This expansion is similar, but not identical, to a spherical harmonic expansion in the velocity space angles θ and ϕ. In (5) $f_p(v,\mathbf{r},t)$ is a pth-order tensor that is a function of speed v only and $\hat{\mathbf{v}} = \hat{\mathbf{z}}\cos\theta + \hat{\mathbf{x}}\sin\theta\cos\phi + \hat{\mathbf{y}}\sin\theta\sin\phi$ is the velocity unit vector. The components of the tensors $(\hat{\mathbf{v}})^p = \Pi_p\hat{\mathbf{v}}$ serve as the set of orthogonal, angular, basis functions. Finally, $:_p$ represents tensor contraction over p indices. The justification for truncating after $\mathbf{f}_1$ is that e–i collisions act to isotropise 'angular detail' in the electron velocity distribution (generated by temperature and density gradients, etc.) thus the following ordering $f_0 > |\mathbf{f}_1| > |\mathbf{f}_2| > \cdots$ is expected to hold if $L_T, L_n > \overline{\lambda}$. In practice it is found that the $f \sim f_0 + f_1$ approximation accurately yields physical, transport quantities like heat flow and electric current even when $f_0 \sim |\mathbf{f}_1|$ [14]. The isotropic part of the distribution f_0 defines the electron number density and the energy density, n_e and U_e, respectively, in the following way:

$$n_e(x,y,t) = 4\pi\int_0^\infty f_0(v,x,y,t)v^2\,\mathrm{d}v, \tag{6}$$

$$U_e(x,y,t) = 4\pi\int_0^\infty \frac{1}{2}m_e v^2 f_0(v,x,y,t)v^2\,\mathrm{d}v, \tag{7}$$

where $U_e = \frac{3}{2}n_e k_B T_e = \frac{3}{2}P_e$ and P_e is the isotropic electron pressure. Similarly $\mathbf{f}_1$ defines the transport fluxes; the electron current density and total heat flow vector, $\mathbf{j}$ and $\mathbf{q}_T$, respectively, as follows:

$$\mathbf{j}(x,y,t) = -\frac{4\pi e}{3}\int_0^\infty \mathbf{f}_1(v,x,y,t)v^3\,\mathrm{d}v, \tag{8}$$

$$\mathbf{q}_T(x,y,t) = \frac{4\pi}{3}\int_0^\infty \frac{1}{2}m_e v^2\mathbf{f}_1(v,x,y,t)v^3\,\mathrm{d}v. \tag{9}$$

By inserting the expanded form of f into the VFP equation, multiplying by $(\hat{\mathbf{v}})^p$ and integrating over the velocity angles θ and ϕ a set of coupled equations for the evolution of the f_p can be obtained [39]. The first two of these are,

$$\frac{\partial f_0}{\partial t} + \frac{v}{3}\nabla\cdot\mathbf{f}_1 - \frac{e/m_e}{3v^2}\frac{\partial}{\partial v}\left(v^2\mathbf{E}\cdot\mathbf{f}_1\right) = \frac{\nu'_{ee}}{v^2}\frac{\partial}{\partial v}\left[C(f_0)f_0 + D(f_0)\frac{\partial f_0}{\partial v}\right], \tag{10}$$

$$\frac{\partial \mathbf{f}_1}{\partial t} + v\nabla f_0 - \frac{e\mathbf{E}}{m_e}\frac{\partial f_0}{\partial v} - \frac{e}{m_e}(\mathbf{B}\times\mathbf{f}_1) + g(\mathbf{f}_2) = -\nu_{ei}\mathbf{f}_1 + C_{ee1}(f_0,\mathbf{f}_1), \tag{11}$$

where $\nu_{ei} = YZ^2 n_i \ln\Lambda_{ei}/v^3$ is the e–i angular scattering frequency, $\nu'_{ee} = Y\ln\Lambda_{ee}$ and $Y = 4\pi(e^2/4\pi\epsilon_0 m_e)^2$. $\ln\Lambda_{ei}$ and $\ln\Lambda_{ee}$ are the Coulomb logarithms for e–i and e–e scattering. The Rosenbluth coefficients $C(f_0)$ and $D(f_0)$ will be given below. We ignore the e–e collision term C_{ee1} in the equation for $\partial_t\mathbf{f}_1$ which is known as the Lorentz approximation and is valid for high Z. Using the diffusion approximation, i.e., $\mathbf{f}_p = 0$ for $p > 1$, means that the term

$$g(\mathbf{f}_2) = \left[\frac{2}{5}v\nabla\cdot\mathbf{f}_2 - \frac{2e}{5m_e v^3}\frac{\partial}{\partial v}(v^3\mathbf{E}\cdot\mathbf{f}_2)\right]$$

in Eq. (11) can be neglected and the equations for $\partial_t\mathbf{f}_2$, $\partial_t\mathbf{f}_3$, etc. need not be considered. By leaving out $\mathbf{f}_2$ effects due to electron viscosity and anisotropic electron pressure are neglected.

2.2. Normalisations

The scheme used involves normalising quantities with respect to characteristic values for a 'reference material' with electron temperature T_{e0}, ion number density n_{i0}, ionisation number Z_0 and electron number density $n_{e0} = Z_0 n_{i0}$. Thus in particular, velocity/speed is normalised to the electron thermal speed corresponding to T_{e0} defined as $v_n = \sqrt{2k_B T_{e0}/m_e}$, time is normalised to the electron–ion 90° scattering time $\tau_n = v_n^3/(YZ_0^2 n_{i0}\ln\lambda_{ei0})$ for a thermal electron moving through the reference material and length is normalised to the thermal, e–i mean-free-path which is $\lambda_n = v_n\tau_n$. The full set of normalisations is

$$\begin{aligned}
&\tilde{v} = \frac{v}{v_n}, \quad \tilde{t} = \frac{t}{\tau_n}, \quad \tilde{x} = \frac{x}{\lambda_n},\\
&\tilde{\partial}_v = v_n\partial_v, \quad \tilde{\partial}_t = \tau_n\partial_t, \quad \tilde{\nabla} = \lambda_n\nabla,\\
&\tilde{f_p} = \frac{f_p}{n_{e0}v_n^{-3}}, \quad \tilde{\mathbf{E}} = \frac{e\mathbf{E}/m_e}{\lambda_n\tau_n^{-2}}, \quad \tilde{\boldsymbol{\omega}} = \frac{e\mathbf{B}/m_e}{\tau_n^{-1}},\\
&\tilde{U}_e = \frac{U_e}{m_e v_n^2 n_{e0}}, \quad \tilde{\mathbf{j}} = \frac{\mathbf{j}}{e n_{e0} v_n}, \quad \tilde{\mathbf{q}} = \frac{\mathbf{q}}{m_e v_n^3 n_{e0}},\\
&\tilde{n}_i = \frac{n_i}{n_{i0}}, \quad \tilde{Z} = \frac{Z}{Z_0}, \quad \tilde{n}_e = \frac{n_e}{n_{e0}}.
\end{aligned} \tag{12}$$

All equations from now on will be written in terms of the quantities above hence tildes ($\sim$) will be dropped for brevity. Any unnormalised equations/expressions will be pointed out. Where necessary, unnormalised quantities (appearing in an otherwise normalised equation) will be denoted with a wide hat (e.g., $\widehat{Z_0}$).

2.3. Equation set

The full set of equations that needs to be solved in 2-D with magnetic fields and stationary ions using the normalisations above is

$$\frac{\partial f_0}{\partial t} + \frac{v}{3}\nabla\cdot\mathbf{f}_1 - \frac{1}{3v^2}\frac{\partial}{\partial v}\left(v^2\mathbf{E}\cdot\mathbf{f}_1\right) = C_{ee0} + H, \tag{13}$$

$$\frac{\partial \mathbf{f}_1}{\partial t} + v\nabla f_0 - \mathbf{E}\frac{\partial f_0}{\partial v} - \boldsymbol{\omega}\times\mathbf{f}_1 = -\frac{Z^2 n_i}{v^3}\mathbf{f}_1, \tag{14}$$

$$C_{ee0} = \frac{1}{\widehat{Z_0} v^2} \frac{\partial}{\partial v} \left[C(f_0) f_0 + D(f_0) \frac{\partial f_0}{\partial v} \right], \tag{15}$$

$$C(v, \mathbf{r}, t) = 4\pi \int_0^v f_0(u, \mathbf{r}, t) u^2 \, \mathrm{d}u, \tag{16}$$

$$D(v, \mathbf{r}, t) = \frac{4\pi}{v} \int_0^v u^2 \left\{ \int_u^\infty f_0(v', \mathbf{r}, t) v' \, \mathrm{d}v' \right\} \mathrm{d}u, \tag{17}$$

$$\nabla \times \boldsymbol{\omega}(\mathbf{r}, t) = \left(\frac{1}{\delta_c} \right)^2 \mathbf{j} + \left[\left(\frac{1}{c} \right)^2 \frac{\partial \mathbf{E}}{\partial t} \right], \tag{18}$$

$$\nabla \times \mathbf{E}(\mathbf{r}, t) = -\frac{\partial \boldsymbol{\omega}}{\partial t}, \tag{19}$$

$$\mathbf{j}(\mathbf{r}, t) = -\frac{4\pi}{3} \int_0^\infty \mathbf{f}_1(v, \mathbf{r}, t) v^3 \, \mathrm{d}v. \tag{20}$$

In configuration space, these equations are solved on a two-dimensional, rectangular, Cartesian domain. All quantities can vary in the x- and y-directions but are invariant in the z-direction, i.e., $\nabla = \partial_x \hat{\mathbf{x}} + \partial_y \hat{\mathbf{y}}$. The electric field and $\mathbf{f}_1$ vectors lie in the x, y-plane, i.e., $\mathbf{E} = E_x \hat{\mathbf{x}} + E_y \hat{\mathbf{y}}$ and $\mathbf{f}_1 = f_x \hat{\mathbf{x}} + f_y \hat{\mathbf{y}}$, while the magnetic field is oriented in the z-direction; $\mathbf{B} = B_z(x, y, t)\hat{\mathbf{z}}$. Consequently the electric current and heat flow vectors, which are velocity moments of $\mathbf{f}_1$, also lie in the x, y-plane. Using this configuration of fields and plasma temperature and density gradients, transport across the magnetic field and magnetic-field generation by thermal sources, e.g., $\partial_t \mathbf{B} \propto -\nabla n \times \nabla T$, can be addressed. In principle B_x and/or B_y could also be included so long as care is taken that $\nabla \cdot \mathbf{B} = 0$ (which is trivially satisfied for the above configuration) continues to hold and E_z and f_z were included to. Arbitrary profiles can be specified for the electron number density $n_e(x, y) = 4\pi \int_0^\infty f_0 v^2 \, \mathrm{d}v$ and ion number density $n_i(x, y)$ but are time independent because the displacement current and hydrodynamics are neglected. Similarly the ionisation state can vary in x and y but is fixed in time because ionisation dynamics is not considered.

The following things should be pointed out about Eqs. (13)–(20):

- H in Eq. (13) is the laser heating term/operator. The form of this for inverse Bremsstrahlung heating is given in [40].
- $\widehat{Z_0}$ in Eq. (15) is left unnormalised (otherwise it would be unity!).
- δ_c in Eq. (18) is the (normalised) collisionless skin depth and is given by $\tilde{\delta}_c = (c/\omega_{pe})/\lambda_n$ where $\omega_{pe}^2 = n_{e0} e^2 / m_e \epsilon_0$ is the electron plasma frequency.
- the speed of light c in Eq. (18) has been normalised.
- We ignore the logarithmic factors $\ln \Lambda_{ee}(n_e, T_e)/\ln \Lambda_{ei0}$ and $\ln \Lambda_{ei}(Z, n_e, T_e)/\ln \Lambda_{ei0}$ that appear in the e–e and e–i collision terms in the f_0 and $\mathbf{f}_1$ equations, respectively, when they are normalised. The main dependence of the collision frequencies on Z, n and T_e appear through the factor $Z^2 n_i$ in (14) and through (15) and the variation with the logarithmic factors is negligible in comparison.

The normalised magnetic field appearing in (14), (18), and (19) is closely related to the Hall parameter $\omega_g \overline{\tau}$ by $\omega_g \overline{\tau} = (3\sqrt{\pi}/4)\tilde{\omega} \tilde{v}_T^3 / (\tilde{Z}^2 \tilde{n}_i \ln \Lambda_{ei}/\ln \Lambda_{ei0})$ where $\omega_g = eB/m_e$ is the electron gyro-frequency, $\overline{\tau} = (3\sqrt{\pi}/4)\tau_n \tilde{v}_T^3 / (\tilde{Z}^2 \tilde{n}_i \ln \Lambda_{ei}/\ln \Lambda_{ei0})$ is the local, distribution averaged e–i collision time, and $\tilde{v}_T = \sqrt{T_e/T_{e0}}$ is the local, thermal velocity. Values of $\omega_g \overline{\tau} \ll 1$ imply that a typical electron only completes a fraction of a

Larmor orbit before undergoing a large deflection due to Coulomb collisions thus the magnetic field hardly affects transport. $\omega_g \overline{\tau} \gg 1$ signifies a high magnetisation.

We can safely neglect the displacement current in Ampère–Maxwell's law (18) for the collisional and semi-collisional phenomena (with characteristic length and timescales, L and t, satisfying $\overline{\lambda} < L$ and $\overline{\tau} < t$) that IMPACT is designed to address if we limit ourselves to non-relativistic electron temperatures, i.e., $\tilde{c}^2 > 1$, and ensure that $\tilde{\delta}_c \leqslant 1$. (The last requirement can in fact be relaxed slightly since time derivative terms are smaller than the other terms by a factor of approximately $\overline{\lambda}/L$). These two criteria together imply that the electron plasma frequency exceeds the *e–i* collision frequency, so that over the resolvable time and distance scales, electron plasma oscillations are easily able to respond and ensure that the plasma is quasineutral with $n_e \approx Zn_i$ holding to good approximation. Effects arising from the displacement current occur too rapidly and too locally to be resolved and can safely be neglected on the length and timescales of interest. Appropriate ranges of T_{e0} and n_{e0} can easily be deduced from

$$\tilde{\delta}_c \sim \frac{10^3 Z_0 \sqrt{n_{e0}/10^{21}\ \mathrm{cm}^{-3}} \ln \lambda_{ei0}}{(T_{e0}/\mathrm{eV})^2}. \tag{21}$$

At the low temperatures and/or high densities where $\tilde{\delta}_c \gg 1$ the Fokker–Planck treatment of collisions breaks down anyway because the plasma is no longer ideal (i.e., the condition *kinetic energy density* $\gg$ *potential energy density* ceases to be satisfied) with only a small the number of electrons present in the Debye sphere.

3. The numerical scheme

In this section, we describe the implicit, finite difference scheme used to solve Eqs. (13)–(20). This scheme is conservative in terms of electron number density n_e. The electric field, as well as f_0 and $\mathbf{f}_1$, is treated implicitly unlike in previous VFP codes [13–17]. This feature and the inclusion of magnetic field make the alternating-direction-implicit (ADI) approach used to solve the finite difference equations (FDEs) in previous 2-D VFP codes [16] unfeasible here. The addition of *B*-field gives rise to mixed, spatial partial-derivatives which cannot easily be dealt with by ADI. We therefore solve the full matrix equation that arises from implicit differencing of $\mathbf{E}$, f_0, and $\mathbf{f}_1$. Implicit treatment of both the electric field and the electron distribution function, plus solution of the full matrix equation makes the code robust and able to use large time steps, i.e., $\Delta t \gg \tau_{ee}, \tau_{ei}$. In contrast to previous 2-D VFP codes (without *B*-fields) [16] and 1-D VFP codes with magnetic field [17], this scheme includes the electron inertia term which can dramatically reduce the computational effort required to solve the matrix equation.

To begin with we describe how the equations are discretized in time, establishing which quantities in each term are treated implicitly and discussing the iterative technique used to treat the nonlinear terms. This is followed by the specification of the finite difference grid and the location of each quantity on the grid. We then describe how each equation is differenced in the phase space (i.e., x, y, v) dimensions. The x and y boundary conditions are then explained. Finally we explain how $\mathbf{f}_1$ is eliminated from the finite difference version of the VFP equation, how the resulting VFP equation for f_0 and Ampère's law are combined into a sparse matrix and how f_0 and $\mathbf{E}$ are implicitly solved for from the sparse matrix equation.

3.1. Time discretisation

Eqs. (13)–(20) are differenced in time so that f_0, $\mathbf{f}_1$ and $\mathbf{E}$ are treated implicitly while $\boldsymbol{\omega}$ is treated explicitly. The nonlinear terms in both the f_0 and $\mathbf{f}_1$ Eqs. (13) and (14) are dealt with via the method of successive approximations whereby only one of desired quantities in a nonlinear term is made implicit and the other quantities are treated in the FD scheme as a lagged, nonlinear, coefficient. This nonlinear iteration is continued until the solution converges. In the nonlinear Vlasov terms that contain both $\mathbf{E}$ and f_0 (or $\mathbf{f}_1$),

the electric field is chosen to be implicit while the electron distribution is treated as a lagged, nonlinear, coefficient. This is different to previous VFP codes for electron transport in laser–plasmas which have either treated these terms completely explicit [13] or chosen f to be implicit there [15–17]. The Vlasov parts of the VFP equation thus look like,

$$\frac{f_0^{n+1,l+1}-f_0^n}{\Delta t}+\frac{v}{3}\nabla\cdot\mathbf{f}_1^{n+1,l+1}-\frac{1}{3v^2}\frac{\partial}{\partial v}\left(v^2\mathbf{E}^{n+1}\cdot\mathbf{f}_1^{n+1,l}\right)=[C_{ee0}+H]^{n+1}, \tag{22}$$

$$\frac{\mathbf{f}_1^{n+1,l+1}-\mathbf{f}_1^n}{\Delta t}+v\nabla f_0^{n+1,l+1}-\mathbf{E}^{n+1}\frac{\partial f_0^{n+1,l}}{\partial v}-\boldsymbol{\omega}^n\times\mathbf{f}_1^{n+1,l+1}=-\frac{Z^2n_i}{v^3}\mathbf{f}_1^{n+1,l+1}, \tag{23}$$

where index n denotes time, e.g., $f_0^{n+1}=f_0(t_{n+1})$, and the index l indicates the nonlinear iteration number. Notice that the $\partial_t\mathbf{f}_1$ term, representing electron inertial, is retained in (23). For the e–e Fokker–Planck collision operator, Eq. (15), the Chang–Cooper scheme [41] is used. This differences f_0 in the 'drag' term and $\partial_v f_0$ in the 'diffusion' term implicitly while the Rosenbluth coefficients $C(f_0)$ and $D(f_0)$ (integral functions of f_0) are normally treated as lagged, nonlinear, coefficients. In cases where accuracy is not of prime importance or the time step $\Delta t\ll 1$ we sometimes treat the Rosenbluth coefficients explicitly thus saving computational effort. The e–e collision operator looks like

$$C_{ee0}^{n+1}=\frac{1}{\widehat{Z_0}v^2}\frac{\partial}{\partial v}\left[C(f_0)^{n+1,l}f_0^{n+1,l+1}+D(f_0)^{n+1,l}\frac{\partial f_0^{n+1,l+1}}{\partial v}\right]. \tag{24}$$

Epperlein [42] has shown that linearisation of the e–e collision operator (followed by iteration) has some advantages over the simpler method used here. It ensures that when C_{ee0} is appropriately differenced in v e–e collisions exactly conserve energy even after only 1 nonlinear iteration rather than as $l\to\infty$ as is the case when using lagged nonlinear coefficients. Additionally the linearized method converges to the solution more rapidly when large time steps are used (large means Δt is many e–e collision times). The disadvantage is that $C(f_0)$ and $D(f_0)$ need to be treated implicitly which complicates the scheme and greatly increases the density of the sparse matrix. Because self-consistent addition of a B-field to a 2-D VFP code and the implicit treatment of $\mathbf{E}$ are already complex tasks which gives rise to a large sparse matrix and because it was not known *a priori* how well a 2-D VFP code with B-field would work with very large Δt, the simpler nonlinear iteration technique was chosen.

The VFP equation is solved implicitly for f_0 and $\mathbf{f}_1$ and $\mathbf{E}$ at the new time t_{n+1} using the following *current constraint* to ensure that the updated distribution yields a current that is consistent with Ampère's law

$$\mathbf{j}^{n+1,l+1}=-\frac{4\pi}{3}\int_0^\infty\mathbf{f}_1^{n+1,l+1}v^3\,\mathrm{d}v=\delta_c^2(\nabla\times\boldsymbol{\omega}^n). \tag{25}$$

This current constraint together with the implicit treatment of $\mathbf{E}$ completely overcomes the problems in maintaining quasineutrality [16] encountered with previous VFP codes. The last step in advancing the solution to time t_{n+1} is to update the magnetic field via Faraday's law using the implicitly solved for electric field

$$\nabla\times\mathbf{E}^{n+1}=-\left(\frac{\boldsymbol{\omega}^{n+1}-\boldsymbol{\omega}^n}{\Delta t}\right). \tag{26}$$

It should be noted that when starting a time step the nonlinear iteration is initiated with $l=0$ and that $f_0^{n+1,0}=f_0^n$ and $\mathbf{f}_1^{n+1,0}=\mathbf{f}_1^n$. Also note that $\mathbf{E}^{n+1}$ does change as the nonlinear iteration proceeds even though the '$l+1$' superscript has been omitted. In the rest of this paper, the nonlinear iteration index will be omitted for brevity and the implicitly differenced occurrences of f_0 and $\mathbf{f}_1$ will just use '$n+1$' while lagged, nonlinear, matrix coefficients will use '$n*$' (rather than '$n+1,l$').

3.2. The grid and placement of quantities

The equations are differenced over a volume of the x, y, v phase space defined by $x_{\min} \leqslant x \leqslant x_{\max}$, $y_{\min} \leqslant y \leqslant y_{\max}$ and $0 \leqslant v \leqslant v_{\max}$. This computational domain is divided up into $nx \times ny \times nv$ cells with nx cells fitting across the grid in the x-direction, etc. This grid can be nonuniform, i.e., the cell widths can vary across the domain in each direction. The nx cell widths in the x-direction are defined by Δx_i for integer $i = 1, \ldots, nx$, and similarly the y and v cell widths are Δy_j and Δv_k, respectively. The $nx + 1$ x-coordinates of the cell boundaries are denoted by $x_{i+1/2}$ for $i = 0, 1, \ldots, nx$ and include the edges of the computational domain; $x_{1/2} = x_{\min}$ and $x_{nx+1/2} = x_{\max}$. The nx x-coordinates of the cell centres x_i for $i = 1, \ldots, nx$ lie *half way* between the adjacent cell boundaries. Finally the $nx - 1$ separations between cell centres (internal to the domain) are $\Delta x_{i+1/2} = x_{i+1} - x_i$ where $i = 1, \ldots, nx - 1$. The positions and separations of cell boundaries and cell centres are similarly defined in the y- and v-directions. It is worth emphasising that the index scheme adopted here is *cell centre based*. When implementing the boundary conditions ghost cells (external to the domain) are used which have x-positions x_0 and x_{nx+1}. Hence $\Delta x_{1/2}$ and $\Delta x_{nx+1/2}$ are also defined and used. Boundary conditions will be discussed in more detail in Sections 3.5 and 3.7.

The simulation quantities are placed in the following way. Along the velocity direction of phase space the scalar and vector distribution functions are located at cell centres. In the spatial dimensions, f_0 and ω are placed at cell centres while *both components* of $\mathbf{f}_1$ and $\mathbf{E}$ are placed at the midpoints of each of the 4 edges which define the cell in the x–y-directions, as depicted in Fig. 1. It is worth defining a notation to distinguish between points lying on the x-cell boundaries and those lying on y-cell boundaries. For example, f_y located on an x-cell boundary will be written as f_y^X while E_y on a y-cell boundary is E_y^Y. The set of points on the x and y-cell boundaries are defined by

$$\begin{aligned} \mathbf{r}_{i,j}^X &= \hat{\mathbf{x}} x_{i+\frac{1}{2}} + \hat{\mathbf{y}} y_j, \quad i = 0, 1, \ldots, nx, \;\; j = 1, \ldots, ny, \\ \mathbf{r}_{i,j}^Y &= \hat{\mathbf{x}} x_i + \hat{\mathbf{y}} y_{j+\frac{1}{2}}, \quad i = 1, \ldots, nx, \;\; j = 0, 1, \ldots, ny, \end{aligned} \tag{27}$$

respectively. The spatial placement of the quantities as shown in Fig. 1 is chosen to enable formulation of a conservative scheme and to ensure that electron momentum is accurately treated when $B \neq 0$.

Having established the FD grid and placement of quantities we now define the full index notation that will be used in writing the finite difference equations. The discrete values of the distribution function components are written as

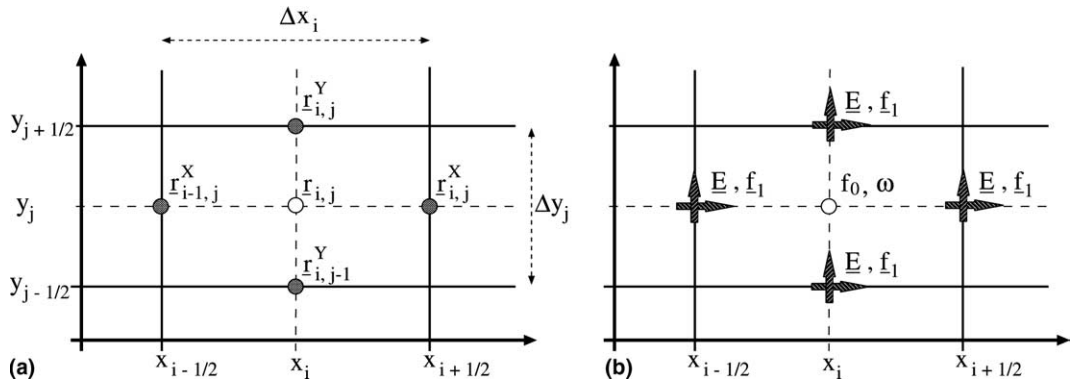

Fig. 1. Example of a spatial cell showing (a) location of x and y-boundary points $\mathbf{r}_{i,j}^X$ and $\mathbf{r}_{i,j}^Y$, and (b) placement of simulation quantities.

$$
\begin{aligned}
(f_0)^n_{i,j,k} &= f_0(x_i, y_j, v_k, t_n),\\
(f_r^X)^n_{i,j,k} &= (f_r)^n_{i+\frac{1}{2},j,k} = f_r(x_{i+\frac{1}{2}}, y_j, v_k, t_n),\\
(f_r^Y)^n_{i,j,k} &= (f_r)^n_{i,j+\frac{1}{2},k} = f_r(x_i, y_{j+\frac{1}{2}}, v_k, t_n),
\end{aligned}
\tag{28}
$$

where $r = \{x, y\}$ is an index over the vector components. Similarly the full index notation for $\mathbf{E}$ and $\boldsymbol{\omega}$ is

$$
\begin{aligned}
\omega^n_{i,j} &= \omega(x_i, y_j, t_n),\\
(E_r^X)^n_{i,j} &= (E_r)^n_{i+\frac{1}{2},j} = E_r(x_{i+\frac{1}{2}}, y_j, t_n),\\
(E_r^Y)^n_{i,j} &= (E_r)^n_{i,j+\frac{1}{2}} = E_r(x_i, y_{j+\frac{1}{2}}, t_n).
\end{aligned}
\tag{29}
$$

The electric current and heat flow vector $\mathbf{j}$ and $\mathbf{q}$ are also located on x and y-boundaries and use the same indexing scheme as $\mathbf{E}$. Note that the two notations for cell boundary quantities, e.g., $(E_r^X)^n_{i,j}$ and $(E_r)^n_{i+1/2,j}$, will both be used in the following.

3.3. The $\boldsymbol{f}_1$ equation

The finite difference form for the rth component of the $\mathbf{f}_1$ equation at location $\mathbf{r}^b_{i,j}$, where $b = \{X, Y\}$ denotes the cell boundary, is

$$
(f_r^b)^{n+1}_{i,j,k} = \left[\chi^n_k \sum_{q=\{x,y\}} \left(\delta_{rq} + \epsilon_{rzq}\omega^n \tau'_k\right)\Big\{ - v_k \left(\nabla_q f_0\right)^{n+1}_k + E^{n+1}_q (\partial_v f_0)^{n*}_k + (f_q)^n_k/\Delta t\Big\}\right]^b_{i,j}, \tag{30}
$$

where

$$
\chi^{b,n}_{i,j,k} = \frac{\tau'_k}{1 + (\omega^{b,n}_{i,j}\tau'_k)^2}, \quad \tau'_k = \left[\frac{1}{\Delta t} + \frac{1}{\tau(v_k)}\right]^{-1}, \tag{31}
$$

$\tau(v_k) = v_k^3/(Z^2 n_\mathrm{i})$ is the e–i scattering time, and δ_{qr} and ϵ_{qrz} are the Kronecker delta function and Levi–Civita symbol, respectively. χ represents how magnetisation and collisions affect the ability of electrons of velocity v_k at position $\mathbf{r}^b_{i,j}$ to contribute to transport. Electron inertia appears through the term in Δt in (31). $\omega^{b,n}_{i,j}$, the value of the B-field on the b-boundary, is obtained by linear interpolation from the adjacent cell centres,

$$
\begin{aligned}
\omega^X_{i,j} &= \omega_{i+\frac{1}{2},j} = (1 - \mu_{i+\frac{1}{2}})\omega_{i+1,j} + \mu_{i+\frac{1}{2}}\omega_{i,j},\\
\omega^Y_{i,j} &= \omega_{i,j+\frac{1}{2}} = (1 - \mu_{j+\frac{1}{2}})\omega_{i,j+1} + \mu_{j+\frac{1}{2}}\omega_{i,j},
\end{aligned}
\tag{32}
$$

where $\mu_{i+\frac{1}{2}} = (x_{i+1} - x_{i+\frac{1}{2}})/\Delta x_{i+\frac{1}{2}}$ and $\mu_{j+\frac{1}{2}} = (y_{j+1} - y_{j+\frac{1}{2}})/\Delta y_{j+\frac{1}{2}}$ are the interpolation weights. Note that Eq. (30) is obtained by eliminating $\boldsymbol{\omega} \times \mathbf{f}_1^{n+1}$ between Eq. (14) and the equation $\boldsymbol{\omega} \times$ (14).

3.3.1. Differencing of $\partial_v f_0$

The $\mathbf{E}\partial_v f_0$ term is of key importance in achieving overall momentum balance. It describes how the electric field decelerates the energetic, flux carrying electrons that leave a small region of plasma and how it also draws the return current of cold electrons to replace them. This return current in turn ensures that the plasma stays quasineutral. We use either forward differencing or centred differencing for this term

$$\left(\frac{\partial f_0}{\partial v}\right)^{b,n*}_{i,j,k} = \left[\frac{(f_0)_{k+1} - (f_0)_k}{\Delta v_k}\right]^{b,n*}_{i,j} \quad \text{or} \tag{33}$$

$$= \left[\frac{(f_0)_{k+1} - (f_0)_{k-1}}{\Delta v_{k+1/2} + \Delta v_{k-1/2}}\right]^{b,n*}_{i,j}, \tag{34}$$

where the value of f_0 at the b-boundary is obtained via the same linear interpolation procedure used to for the B-field (i.e., (32) but with ω replaced by f_0). Because f_0 is not defined at velocity cell boundaries, $(f_0)_{k+1}$ and $(f_0)_{k-1}$ rather than $(f_0)_{k+1/2}$ and $(f_0)_{k-1/2}$ are used in the centred case. It was originally anticipated that forward differencing (33) would be more robust than centred (34). The rationale for this is that $\mathbf{E}\partial_v f_0$ is a dominant term for hot electrons which are decelerated by the electric field. The $\partial_v f_0$ term yields an advective term when the f_0 and $\mathbf{f}_1$ equations are combined, i.e., $\partial_t f_0 \propto E^2 \partial_v f_0$. Eq. (33) would then be consistent with advection of these electrons towards $v = 0$ in an upwind manner which is low order but known to be stable. In practice centred differencing (34) has proved to be as reliable as forward differencing (even for highly nonlinear, non-equilibrium situations) and is $O(\Delta v^2)$ accurate rather than $O(\Delta v)$. The implicit diffusion in v arising from the FP collision term amongst other things is probably what renders the choice of differencing for the $\partial_v f_0$ term unimportant for stability.

3.3.2. Differencing of ∇f_0

Both components of ∇f_0 use centred differencing. $(\partial_x f_0)^X$ and $(\partial_y f_0)^Y$ are approximated by 2-point differences which are accurate to $O(\Delta x^2)$ and $O(\Delta y^2)$, respectively. $(\partial_y f_0)^X$ and $(\partial_x f_0)^Y$ use 4 points owing for the need to linearly interpolate f_0 to the cell boundaries before taking the derivative and have a truncation error of $O(\Delta x^2 + \Delta y^2)$. The equations for $(\nabla_q f_0)^b$ are,

$$\begin{aligned}
(\nabla_q f_0)^X_{i,j} &= (\nabla_q f_0)_{i+\frac{1}{2},j} = \delta_{qx}\frac{\left[(f_0)_{i+1} - (f_0)_i\right]_{j,k}}{\Delta x_{i+\frac{1}{2}}} + \delta_{qy}\frac{\left[(f_0)_{j+1} - (f_0)_{j-1}\right]_{i+\frac{1}{2},k}}{\Delta y_{j+\frac{1}{2}} + \Delta y_{j-\frac{1}{2}}},\\
(\nabla_q f_0)^Y_{i,j} &= (\nabla_q f_0)_{i,j+\frac{1}{2}} = \delta_{qy}\frac{\left[(f_0)_{j+1} - (f_0)_j\right]_{i,k}}{\Delta y_{j+\frac{1}{2}}} + \delta_{qx}\frac{\left[(f_0)_{i+1} - (f_0)_{i-1}\right]_{j+\frac{1}{2},k}}{\Delta x_{i+\frac{1}{2}} + \Delta x_{i-\frac{1}{2}}}.
\end{aligned} \tag{35}$$

3.4. Vlasov part of the f_0 equation

The Vlasov terms in the f_0 equation are differenced in the following way:

$$\begin{aligned}
\text{LHS of (13)} = &\left[\frac{f_0^{n+1} - f_0^n}{\Delta t}\right]_{i,j,k} + \frac{v_k}{3}\left[\frac{\left\{(f_x)_{i+\frac{1}{2}} - (f_x)_{i-\frac{1}{2}}\right\}_{j,k}}{\Delta x_i} + \frac{\left\{(f_y)_{j+\frac{1}{2}} - (f_y)_{j-\frac{1}{2}}\right\}_{i,k}}{\Delta y_j}\right]^{n+1}\\
&- \frac{1}{3v_k^2}\sum_{r=\{x,y\}}\left[E_r^{n+1}\left(\frac{\partial v^2 f_r}{\partial v}\right)^{n*}_k\right]_{i,j}.
\end{aligned} \tag{36}$$

The last term, the so-called Ohmic heating term, involves $\mathbf{E}$ and $\mathbf{f}_1$ at the x–y cell centre. There is some freedom in how E_r and f_r are interpolated from the cell boundaries to the cell centre. Either (1) E_x and f_x at the 'left' and 'right' x-cell boundaries and E_y and f_y at the 'upper' and 'lower' y-cell boundaries can be linearly interpolated to the cell centre, (2) the converse can be done; E_x and f_x at the y-cell boundaries and E_y and f_y at the x-cell boundaries can be linearly interpolated to the cell centre, or (3) both (1) and (2) can be combined. For instance the interpolation used in method (1) is given by

$$(E_x f_x)_{i,j} = \frac{1}{2}\left\{(E_x f_x)_{i+\frac{1}{2}} + (E_x f_x)_{i-\frac{1}{2}}\right\}_j,$$
$$(E_y f_y)_{i,j} = \frac{1}{2}\left\{(E_y f_y)_{j+\frac{1}{2}} + (E_y f_y)_{j-\frac{1}{2}}\right\}_i, \tag{37}$$

where the construction of the grid makes the necessary linear interpolation weights equal 1/2. In theory method (2) complements how $\nabla \times \mathbf{E}$ is differenced in Faraday's law (see Section 3.6) thereby ensuring consistency between changes in magnetic energy and thermal energy in a cell. Since Ohmic heating typically changes the electron temperature much more slowly than heat flow we find that the choice of interpolation is not crucial.

3.4.1. Differencing of $\partial_v(v^2 \boldsymbol{f}_1)$

This term is differenced in the following way:

$$\left(\frac{\partial v^2 f_r}{\partial v}\right)^{n*}_{i,j,k} = \left[\frac{v^2_{k+\frac{1}{2}}(f_r)_{k+1} - v^2_{k-\frac{1}{2}}(f_r)_k}{\Delta v_k}\right]^{n*}_{i,j}. \tag{38}$$

Because f_r is not defined at velocity cell boundaries, $(f_r)_{k+1}$ and $(f_r)_k$ rather than $(f_r)_{k+\frac{1}{2}}$ and $(f_r)_{k-\frac{1}{2}}$ are used. f_r is displaced to higher velocity which provides consistency with the displacement of f_0 in the $\partial_v f_0$ term when forward differenced. (Note that centred differencing of $\partial_v f_0$ is more recent than forward, and a corresponding centre differenced version of the $\partial_v(v^2\mathbf{f}_1)$ has yet to be implemented.) Notice that $v^2_{k+\frac{1}{2}}$ and $v^2_{k-\frac{1}{2}}$ rather than v^2_{k+1} and v^2_k are used though. The differencing in (38) ensures numerical conservation of electron density as will be shown in Section 3.9 but does not enforce zero Ohmic heating when $\mathbf{j} = 0$. We find that the velocity differencing of $\partial_v(v^2\mathbf{f}_1)$ rather than the spatial interpolation of $\mathbf{E}\cdot\mathbf{f}_1$ to the cell centre is the dominant source of numerical error in this term and is the chief cause of energy non-conservation overall.

3.5. Fokker–Planck part of the f_0 equation

The *e–e* collision term in the f_0 equation is differenced using a scheme devised by Chang and Cooper [41] together with a modification due to Langdon [42,43]. Two important properties of the *e–e* collision term (15) are that it conserves electron number and energy densities. The Chang–Cooper differencing scheme conserves numerical number density, while Langdon's modification makes the scheme energy conservative too. The Chang–Cooper scheme has widely been used before [13–17] since it is implicit and has the following desirable properties in addition to density conservation; in the absence of rounding errors it ensures that (i) *e–e* collisions relax f_0 exactly to a Maxwellian (in the absence of the perturbing flux $\mathbf{f}_1$) and (ii) f_0 remains positive for all v. Ensuring f_0 relaxes accurately to f_M is extremely important when considering magnetic field generation otherwise spurious *B*-fields can be produced [8]. Negative f_0 would simply be unphysical.

Following Chang–Cooper and Langdon the *e–e* collision operator is differenced in conservative form in v (at each spatial cell centre),

$$(C_{ee0})^{n+1}_{i,j,k} = \frac{1}{\widehat{Z_0} v_k^2}\left[\frac{F_{k+\frac{1}{2}} - F_{k-\frac{1}{2}}}{\Delta v_k}\right]^{n+1}_{i,j}, \tag{39}$$

where F is a generalised flux located at the velocity cell boundaries and is given by

$$F^{n+1}_{i,j,k+\frac{1}{2}} = \left\{C^{n*}_{k+\frac{1}{2}}(f_0)^{n+1}_{k+\frac{1}{2}} + D^{n*}_{k+\frac{1}{2}}\frac{(f_0)^{n+1}_{k+1} - (f_0)^{n+1}_k}{\Delta v_{k+\frac{1}{2}}}\right\}_{i,j}. \tag{40}$$

Obtaining F requires that f_0 be implicitly known on the velocity cell boundaries. A key step of the Chang–Cooper scheme is the interpolation of f_0 from velocity cell centres to velocity cell boundaries using special 'equilibrium seeking' weights $\delta_{k+\frac{1}{2}}$

$$(f_0)^{n+1}_{k+\frac{1}{2}} = (1-\delta_{k+\frac{1}{2}})(f_0)^{n+1}_{k+1} + \delta_{k+\frac{1}{2}}(f_0)^{n+1}_{k}, \tag{41}$$

$$\delta_{k+\frac{1}{2}} = \frac{1}{W_{k+\frac{1}{2}}} - \frac{1}{\exp(W_{k+\frac{1}{2}})-1}, \tag{42}$$

$$W_{k+\frac{1}{2}} = \Delta v_{k+\frac{1}{2}}\left(C^{n*}_{k+\frac{1}{2}}/D^{n*}_{k+\frac{1}{2}}\right). \tag{43}$$

The coefficient of dynamic friction in differenced form is simply

$$C^{n*}_{k+\frac{1}{2}} = 4\pi\sum_{l=1}^{k}(f_0)^{n*}_l v_l^2 \Delta v_l. \tag{44}$$

Langdon's modification, which allows e–e collisions to numerically conserve energy, involves differencing D the coefficient of dynamic diffusion in the form given in Eq. (17) rather than the (analytically but not numerically) equivalent form $D = (4\pi/3)[v^{-1}\int_0^v f_0(u)u^4\,\mathrm{d}u + v^2\int_u^\infty f_0(u)u\,\mathrm{d}u]$ normally found in the literature. In conservative difference form D is

$$\begin{aligned} D^{n*}_{k+\frac{1}{2}} &= \frac{4\pi}{v^*_{k+\frac{1}{2}}}\sum_{l=1}^{k} v_l^2\left\{\sum_{m=l}^{nv-1}(f_0)^{n*}_{m+\frac{1}{2}} v^*_{m+\frac{1}{2}}\Delta v_{m+\frac{1}{2}}\right\}\Delta v_l \quad (k=1,\ldots,nv-1),\\ D^{n*}_{1/2} &= 0, \qquad D^{n*}_{nv+\frac{1}{2}} = 0, \end{aligned} \tag{45}$$

where $v^*_{m+\frac{1}{2}} = (v_{m+1}-v_m)/2$ is slightly different from the cell boundary definition given in Section 3.2 which is $v_{k+\frac{1}{2}} = \sum_{l=1}^{k}\Delta v_l$.

In the finite difference approximation the electron number and energy densities are defined by

$$(n_e)_{i,j} = 4\pi\sum_{k=1}^{nv}(f_0)_{i,j,k} v_k^2 \Delta v_k, \tag{46}$$

$$(U_e)_{i,j} = \frac{4\pi}{2}\sum_{k=1}^{nv}(f_0)_{i,j,k} v_k^4 \Delta v_k. \tag{47}$$

Insisting that the generalised flux vanishes at $v_{1/2}$ and $v_{nv+\frac{1}{2}}$, the boundaries of the velocity domain, immediately implies numerical conservation of electron density. Vanishing of the flux in turn imposes boundary conditions in the v-direction; $C_{1/2}=0$, $D_{1/2}=0$, $(f_0)_{nv+\frac{1}{2}}=0$ (which needs $(f_0)_{nv+1}=0$ and $\delta_{nv+\frac{1}{2}}=0$) and $D_{nv+\frac{1}{2}}=0$. Proof that the scheme conserves energy density is too involved to give here and the reader is referred to [42,43] for further details.

Operators for collisional laser heating can be incorporated in the Fokker–Planck e–e collision term. We use the inverse Bremsstrahlung operator derived in [40] which tends to distort f_0 away from Maxwellian, flattening it out in the vicinity of $v=0$. Heating operators can be spliced seamlessly into the existing difference formulation for $(C_{ee0})^{n+1}_{i,j,k}$ as described in [16]. We also use a variation on inverse Bremsstrahlung which adds a contribution of $D_0 v^2$ onto the Rosenbluth diffusion coefficient (45). In the absence of transport (i.e., no spatial gradients or electric field) this operator increases the electron temperature at a rate $\partial_t T_e = 3D_0/\widehat{Z_0}$, keeping f_0 nearly Maxwellian all the while.

3.6. Maxwell's equations and the current constraint

In the finite difference approximation, the electric current is defined as

$$\mathbf{j}^b_{i,j} = -\frac{4\pi}{3}\sum_{k=1}^{nv}(\mathbf{f}^b_1)_{i,j,k}v_k^3\Delta v_k. \tag{48}$$

In difference form the rth component of Ampère's law at x–y cell boundary point $\mathbf{r}^b_{i,j}$ is

$$\left[(\nabla\times\boldsymbol{\omega})^b_r\right]^n_{i,j} = \epsilon_{rqz}(\nabla_q\omega)^{b,n}_{i,j} = -\frac{4\pi}{3\delta_c^2}\sum_{k=1}^{nv}(f^b_r)^{n+1}_{i,j,k}v_k^3\Delta v_k, \tag{49}$$

where the components of the gradient of ω at the cell boundary, $(\nabla_q\omega)^b$, are given by (35) with f_0 replaced by ω. Note that $(f^b_r)^{n+1}_{i,j,k}$ is related to $\mathbf{E}$, f_0 and ω through (30). This 'current constraint' ensures that the implicitly obtained $\mathbf{f}_1^{n+1}$ exactly yields the current at time t_n. This equation effectively serves as an Ohm's law since it is responsible for relating $\mathbf{E}$, $\mathbf{j}$ and gradients in density and pressure together in a way that yields the correct momentum balance in the presence of a magnetic field. On a uniform spatial grid it can be shown that $\epsilon_{rqz}(\nabla_q\omega)^b_{i,j} = (j^b_r)_{i,j}/\delta_c^2$ ensures that

$$[\nabla\cdot\mathbf{j}]^{n+1}_{i,j} = \frac{\left\{(j_x)_{i+\frac{1}{2}}+(j_x)_{i-\frac{1}{2}}\right\}^{n+1}_j}{\Delta x}+\frac{\left\{(j_y)_{j+\frac{1}{2}}+(j_y)_{j-\frac{1}{2}}\right\}^{n+1}_i}{\Delta y}=0 \tag{50}$$

(where Δx and Δy can be different) so that $\partial_t n_e = 0$ exactly. On a non-uniform grid $\nabla\cdot\mathbf{j}\neq 0$ is possible.

Faraday's law in difference form is

$$\frac{\{\omega^{n+1}-\omega^n\}_{i,j}}{\Delta t} = \frac{\left\{(E_x)_{j+\frac{1}{2}}-(E_x)_{j-\frac{1}{2}}\right\}^{n+1}_i}{\Delta y_j}-\frac{\left\{(E_y)_{i+\frac{1}{2}}-(E_y)_{i-\frac{1}{2}}\right\}^{n+1}_j}{\Delta x_i}. \tag{51}$$

3.7. Spatial boundary conditions

Reflective, periodic, and fixed boundary conditions are implemented in the code and can independently be used in the x- and y-directions. Periodic boundary conditions are implemented in the normal way and ensure that, e.g., $\mathbf{E}|_{x_{max}} = \mathbf{E}|_{x_{min}}$. With fixed boundary conditions, $f_0(v)$ and ω are specified in each of the ghost cells just outside the relevant boundary rather than being treated implicitly. Two variations of reflective boundary conditions can be used. In both cases the gradients of the scalar quantities f_0, n_i and Z across the boundary are zero, i.e., $\hat{\mathbf{s}}\cdot\nabla f_0 = 0$, where $\hat{\mathbf{s}}$ is the unit vector normal to boundary. The difference lies in how the magnetic field is treated and whether fluxes are allowed across the domain boundaries. In one case the B-field is zero on the boundary and all components of fluxes and the E-field component normal to the boundary vanish. Fluxes and a component of the E-field along the boundary are possible though. Of course there can be a B-field gradient across the boundary generated by the current flowing along it. In the second case, there is no B-field gradient across the boundary and no current along the boundary but fluxes and an E-field component normal to the boundary are now possible. Note that while the current is restricted to being normal to the boundary $\mathbf{E}$, $\mathbf{q}$ and $\mathbf{f}_1(v)$ are free to cross it at any angle in this case.

3.8. Formation and solution of the sparse matrix

The finite difference equations which are solved together in order to obtain the implicitly differenced quantities f_0^{n+1}, $\mathbf{f}_1^{n+1}$ and $\mathbf{E}^{n+1}$ are (30), (36), (39), and (49). Solution of these equations is achieved by

forming a sparse matrix from the equations and then using a matrix solver. In order to reduce the dimension of this sparse matrix $\mathbf{f}_1^{n+1}$ is eliminated from the set of equations by substituting Eq. (30) into (36), the Vlasov part of the f_0 FDE, and (49) the current constraint (Ampères law). After elimination of $\mathbf{f}_1^{n+1}$ the VFP equation for the evolution of f_0 at point x_i, y_j, v_k in phase space, in a compact matrix coefficient form, is

$$G_{p,q,s}(x_i, y_j, v_k) f_0(x_{i+p}, y_{j+q}, v_{k+s}, t_{n+1}) + H_{r,b,m,n}(x_i, y_j, v_k) E_r^b(x_{i+m}, y_{j+n}, t_{n+1}) = C(x_i, y_j, v_k), \tag{52}$$

where $p, q, s = \{-1, 0, 1\}$ and $m, n = \{-1, 0\}$ are finite difference offsets and $r, b = \{x, y\}$. Summation over the indices p, q, s and m, n is implied in (52). Similarly the current constraint for j_r at $\mathbf{r}_{i,j}^b$ becomes

$$M_{c,d,s}(r, b, x_i, y_j) f_0(x_{i+c}, y_{j+d}, v_s, t_{n+1}) + N_g(r, b, x_i, y_j) E_g^b(x_i, y_j, t_{n+1}) = D(r, b, x_i, y_j), \tag{53}$$

where $c, d = \{-1, 0, 1\}$ are finite difference offsets, $s = \{1, \ldots, nv\}$ effects integration over v and $g = \{x, y\}$, and where summation over c, d, s, g is implied. Note that the matrix coefficients G, H, M and N vary with position on the grid. M and N also vary with vector component r. Also some elements of G, H and M are always zero; $G_{p,q,\pm 1} = 0$ for $p \neq 0$ and $q \neq 0$, $H_{r,X,m,-1} = H_{r,Y,-1,n} = 0$ and $M_{-1,-1,s} = 0$.

Together (52) and (53) form a set of nd linear algebraic equations for the nd unknowns $f_0(x_i, y_j, v_k, t_{n+1})$ and $E_r^b(x_i, y_j, t_{n+1})$, where $nd = nc + 2 \times [2(nx \times ny) + nx + ny]$ and $nc = nx \times ny \times nv$. Each of these linear algebraic equations forms one row of the matrix equation. Symbolically, this matrix equation can be written as $\mathbf{A}^{n*} \cdot \mathbf{x}^{n+1} = \mathbf{B}^n$, where $\mathbf{x}^{n+1}$ is the vector of nd unknowns to be solved for. A realisation of this sparse matrix when $nx \times ny \times nv = 4 \times 4 \times 4$ is shown in Fig. 2.

The diagonal elements of the matrix $\mathbf{A}^{n*}$ are $G_{0,0,0}(x_i, y_j, v_k)$ for $i = \{0, \ldots, nx\}$, $j = \{1, \ldots, ny\}$ and $k = \{1, \ldots, nv\}$, and $N_r(r, b, x_{i'}, y_{j'})$. The defined ranges of i' and j' for $b = \{X, Y\}$ were given in (27). By eliminating $\mathbf{f}_1^{n+1}$ the dimension of the sparse matrix is reduced from approximately $5 \times nc$ while the total number of non-zero matrix elements decreases from approximately $51 \times nc$ to $43 \times nc$. In fact the element count of the unreduced sparse matrix would rise to $55 \times nc$ if the Ohmic heating term in the f_0 FDE were to use the value of $(E_r)^{n+1}$ on all 4 cell boundaries when obtaining the E-field at the cell centre.

Solution of the resulting non-symmetric sparse matrix equation $\mathbf{A}^{n*} \cdot \mathbf{x}^{n+1} = \mathbf{B}^n$ for $\mathbf{x}^{n+1}$ is achieved using the *bi-conjugate gradient stabilised* method [44] with Jacobi preconditioning (also known as diagonal preconditioning). The bi-conjugate gradient stabilised method (Bi-CGSTAB) is an iterative matrix solver. The 'normal' bi-conjugate gradient method (Bi-CG) [45] has also been tried but typically takes three times more iterations than Bi-CGSTAB to converge for a given matrix that arises in this numerical scheme. Once f_0^{n+1} and $(E_r^b)^{n+1}$ have been obtained by solving the matrix equation $\mathbf{f}_1^{n+1}$ has to be calculated using Eq. (30) in order to proceed with the next nonlinear iteration. This is because it appears in the lagged, nonlinear coefficient in the Ohmic heating term (see Eq. (13)) and is thus part of the matrix $\mathbf{A}^{n*}$. The nonlinear iteration is continued until the absolute fractional change in $|\mathbf{x}|$ drops below a specified tolerance. The final step required to advance the solution from t_n to t_{n+1} is to update the magnetic field using Faraday's law (51). It should be noted that IMPACT uses double precision floating point arithmetic (i.e., 64 bit) throughout.

3.9. Conservation properties

Mass and total energy (thermal + magnetic) are the quantities conserved by Eqs. (13)–(20) used by the model. Electron momentum is not conserved but total momentum (electrons + ions + electro-magnetic) would be conserved if ion-motion and the displacement current were included in the model. The continuity equations for mass and total energy (in normalised form) are

$$\partial_t n_e - \nabla \cdot \mathbf{j} = 0, \tag{54}$$

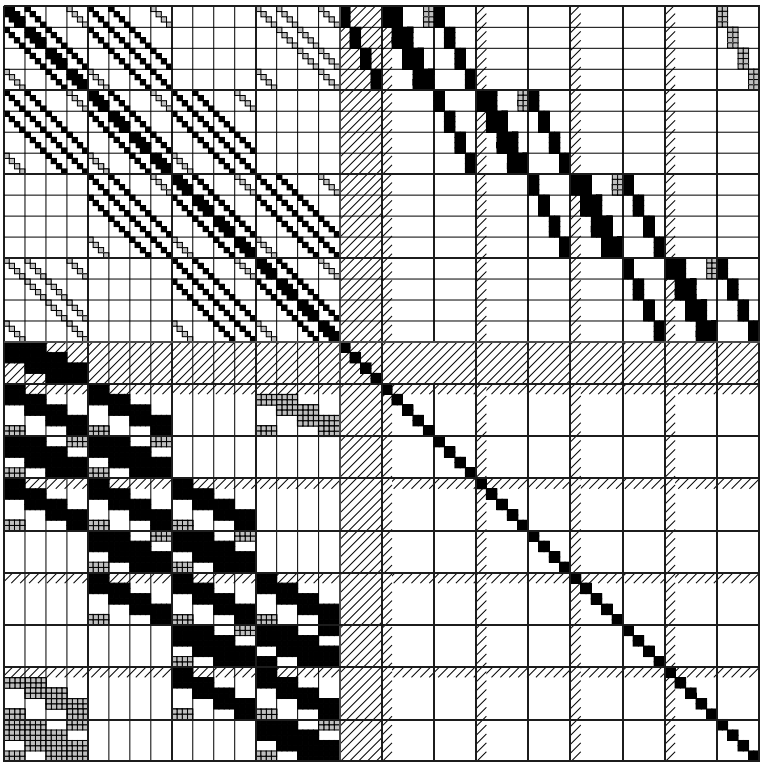

Fig. 2. Sparse matrix for $nx \times ny \times nv = 4 \times 4 \times 4$ with periodic spatial boundary conditions. Rows/columns corresponding to $(f_0)^{n+1}_{i,j,k}$ appear first followed by $(E^b_r)_{i,j}$. The phase space is unravelled in the following order (fastest to slowest varying dimension); v, y, x. For E the ordering of the indices/dimensions across the matrix is (fastest to slowest varying); r (vector component), y, b (cell boundary), x.

$$\partial_t(U_e + U_B) + \nabla \cdot \{\mathbf{q}_\mathrm{T} + \mathbf{S}\} = 0, \tag{55}$$

where $U_B = \omega^2/2\delta_\mathrm{c}^2$ is the magnetic energy density and $\mathbf{S} = (\mathbf{E} \times \boldsymbol{\omega})/\delta_\mathrm{c}^2$ is the Poynting flux. Eqs. (54) and (55) are obtained by taking number density and energy moments of the f_0 equation. The Ohmic heating term in the resulting energy equation $\partial_t U_e + \nabla \cdot \mathbf{q}_\mathrm{T} = \mathbf{E} \cdot \mathbf{j}$ is then converted to $\mathbf{E} \cdot \mathbf{j} = -(\partial_t U_B + \nabla \cdot \mathbf{S})$ by using Ampère's law and Faraday's law. Note that the Ohmic heating term is responsible for conversion of electro-magnetic energy into internal/thermal energy of the electrons (and vice versa). Also, the electric field energy density does not appear in (55) because the displacement current is neglected. Eqs. (54) and (55) show that mass and total energy are conserved in a closed system. Furthermore, because $\mathbf{j} \propto \nabla \times \boldsymbol{\omega}$ the electron number density never changes.

The numerical scheme ensures conservation of mass. It also ensures that the number density remains static when a uniform spatial grid is used. Energy is not exactly conserved though due to the differencing of the Ohmic heating term in the f_0 equation. Numerical conservation of mass can be seen by taking the FD number density moment/sum, defined by Eq. (46), of the differenced Vlasov equation (36) and Fokker–Planck e–e collision term (39) for f_0 which yields

$$\left[\frac{n_\mathrm{e}^{n+1} - n_\mathrm{e}^n}{\Delta t}\right]_{i,j} - (\nabla \cdot \mathbf{j})^{n+1}_{i,j} - \frac{4\pi}{3}\mathbf{E}^{n+1}_{i,j} \cdot \left[v^2_{1/2}(\mathbf{f}^{n*}_1)_1 - v^2_{nv+\frac{1}{2}}(\mathbf{f}^{n*}_1)_{nv+1}\right]_{i,j} = \frac{4\pi}{3\widehat{Z}_0}\left[F_{nv+\frac{1}{2}} - F_{1/2}\right]^{n+1}_{i,j}. \tag{56}$$

Since $v_{1/2}$, $(f_r)_{nv+1}$, $F_{1/2}$, and $F_{nv+\frac{1}{2}}$ all equal zero, the Ohmic heating and Fokker–Planck terms individually sum to zero and the numerical equivalent of (54) is recovered which conserves total mass in the computational domain. The reason why the scheme does not exactly conserve energy can be seen by taking the FD energy sum (defined by (47)) of the f_0 equation. This does not quite yield the discrete analogue of $\partial_t U_e + \nabla \cdot \mathbf{q}_T = \mathbf{E} \cdot \mathbf{j}$. While the terms $\partial_t U_e$ and $\nabla \cdot \mathbf{q}_T$ are recovered, and the numerical Fokker–Planck collision term vanishes [42,43] the Ohmic heating term is not exactly obtained. Doing the energy summation over $(1/3v^2)\partial_v(v^2 f_r)$ followed by rearrangement of the terms (in a way analogous to integration by parts) yields $(j_r)^* = (-4\pi/3)\sum_{k=1}^{nv-1}(f_r)_{k+1}(v^2 v^* \Delta v)_{k+\frac{1}{2}}$, where $v^*_{k+\frac{1}{2}} = (v_{k+1} + v_k)/2$. This is not quite the same as $(j_r) = -(4\pi/3)\sum_{k=1}^{nv}(f_r v^3 \Delta v)_k$, the 'real' numerical current which the scheme ensures equals $\delta_c^2 \nabla \times \boldsymbol{\omega}$, and thus $(j_r)^*$ does not necessarily vanish when $\nabla \times \boldsymbol{\omega} = 0$.

4. Tests

IMPACT has been comprehensively tested to make sure that it correctly recovers phenomena and effects that are known to be described by the equation set (13)–(20). Testing the code is challenging because, in general, analytical solution of the whole equation set is impossible. Most of if not all of the effects that are quantitatively understood and are therefore suitable for testing against make simplifications/assumptions somewhere in their derivation. The tests shown below in Sections 4.1–4.3 compare the code against *classical transport* which is valid in the local/fluid limit since it assumes $f_0 = f_M$. We have developed one test, described in Section 4.4, which tests transport and magnetic field generation beyond the classical limit and works while f_0 is mildly non-Maxwellian. No fully kinetic theory of transport in a collisional magnetised plasma which applies when f_0 is strongly non-Maxwellian exists yet. Understanding what happens in this regime is a prime reason for developing IMPACT. A table of CPU times, memory usage, and the average number of nonlinear iterations required per time step, for representative runs from each test, can be found in Section 4.6.

4.1. Reproducing classical transport

We consider the electric field and heat flux generated by gentle temperature and density gradients (with $L_T, L_n \gg \overline{\lambda}$) in the presence of a strong magnetic field. We show that in this limit (i.e., $L_T, L_n \gg \overline{\lambda}$) the electric field and heat flux obtained from IMPACT agree with those predicted from the well-known classical, electron transport equations of Braginskii [1],

$$\mathbf{E} = -\frac{\nabla P_e}{n_e e} + \frac{\mathbf{j} \times \mathbf{B}}{n_e e} + \boldsymbol{\alpha} \cdot \mathbf{j} - \boldsymbol{\beta} \cdot \nabla T_e, \tag{57}$$

$$\mathbf{q} = -\boldsymbol{\kappa} \cdot \nabla T_e - T_e \boldsymbol{\beta} \cdot \mathbf{j}, \tag{58}$$

where $\boldsymbol{\alpha}$, $\boldsymbol{\beta}$ and $\boldsymbol{\kappa}$ are the electrical resistivity, thermoelectric and thermal conductivity tensors, respectively. These transport coefficients appearing in Ohms law (57) and the heat flow equation (58) are tensor (rather than scalar) quantities because the transport fluxes (e.g., $\mathbf{q}$, $\mathbf{j}$) are not parallel to the driving forces (e.g., ∇T_e, ∇P_e, $\mathbf{E}$) when a magnetic field is present. For instance in the 2-D geometry adopted here with a perpendicular B-field the heat flow driven by a temperature gradient is the sum of two parts, $\mathbf{q} = -\boldsymbol{\kappa} \cdot \nabla T_e = -\kappa_\perp \nabla T_e - \kappa_\wedge \hat{\mathbf{b}} \times \nabla T_e$, one part directed down the temperature gradient and one directed perpendicular to direction of ∇T_e and magnetic field line ($\hat{\mathbf{b}}$ denotes the B-field direction) which is known as the Righi–Leduc heat flow. In classical transport theory, calculation of $\boldsymbol{\alpha}$, $\boldsymbol{\beta}$ and $\boldsymbol{\kappa}$ is achieved using the local approximation whereby $f_0 = f_M$. IMPACT on the other hand dispenses with this approximation so we have to make sure that f_0 does not deviate too far from Maxwellian in order to make a meaningful comparison with classical

transport theory. For this reason f_0 is initialised as a Maxwellian (with the required temperature and density) at each point on the grid. Then, by using a large domain, keeping the perturbations of T, n and Z small in amplitude and evolving the system for a short time we ensure that $f_0 = f_M$ to very good approximation.

The test system has a size of $x_l \times y_l = 5000 \times 5000$ (in normalised units) where $x_l = x_{max} - x_{min}$ is the x-length, etc. It is initialised with the following temperature, density, ionisation number and magnetic field profiles which are depicted in Fig. 3; $\delta T(x,y) = 0.0005[\cos(k_x x) + \cos(k_y y)]$, $\delta n(x,y) = 0.0005[\cos(k_x x) + \cos(k_y\{y - 5000\})]$, $\delta Z(x,y) = 0.02[\cos(k_x\{x - 5000\}) + \cos(k_y y)]$ and $\omega(x,y) = 0.1\cos(k_x\{x - 2500\})\cos(k_y\{y - 2500\})$, where $k_x = \pi/x_l$ and $k_y = \pi/y_l$. Note that $\omega \sim 0.1$ corresponds to quite strong magnetisation. Reflective boundary conditions with $\omega = 0$ on the boundary, $Z_0 = 10$, $\delta_c = 1$, $v_{max} = 8$ and forward differencing of $\mathbf{E}\partial_v f_0$ are used. The inertial term $\partial_t \mathbf{f}_1$ is switched off so that comparison with (57) and (58) can be made but e–e collisions are turned on. Fig. 4 shows the electric field, total heat flow, electric current and error in the E-field at the x-cell-boundaries after a single time step of $\Delta t = 0.1$, when $nx = ny = 48$ and $\Delta v = 1/100$. The total heat flow $\mathbf{q}_T$ includes transport of thermal energy by the drift of electrons and is related to the intrinsic heat flow $\mathbf{q}$ by $\mathbf{q}_T = \mathbf{q} - \mathbf{j}[(5/2)p\mathbf{I} + \mathbf{\Pi}]/n - \mathbf{j}j^2/(2n^3)$ [46]. While the electric current is equal to $\nabla \times \boldsymbol{\omega}$ and is 90° rotationally symmetric about $(x,y) = (2500, 2500)$, this is not quite true for $\mathbf{q}_T$ and $\mathbf{E}$ due to their dependence on T, n and Z (partly through the transport coefficients). Both the heat flow and the electric field are dominated by terms involving $\mathbf{j}$, though the pressure and temperature gradient terms do contribute as well. Cross-field effects are not negligible and give rise to the 'outward swirling' behaviour of $\mathbf{q}_T$ and particularly $\mathbf{E}$. For example, $\alpha_\wedge(\mathbf{j} \times \hat{\mathbf{b}})$ and $\mathbf{j} \times \mathbf{B}$ are responsible for the cross-field effects in the case of $\mathbf{E}$. The reason why the error in the E-field (Fig. 4(d)) is closely reminiscent of the E-field itself is that the code slightly overestimates the electrical resistivity (and the $\mathbf{j} \times \mathbf{B}$ term too). Note that $\mathbf{j}$

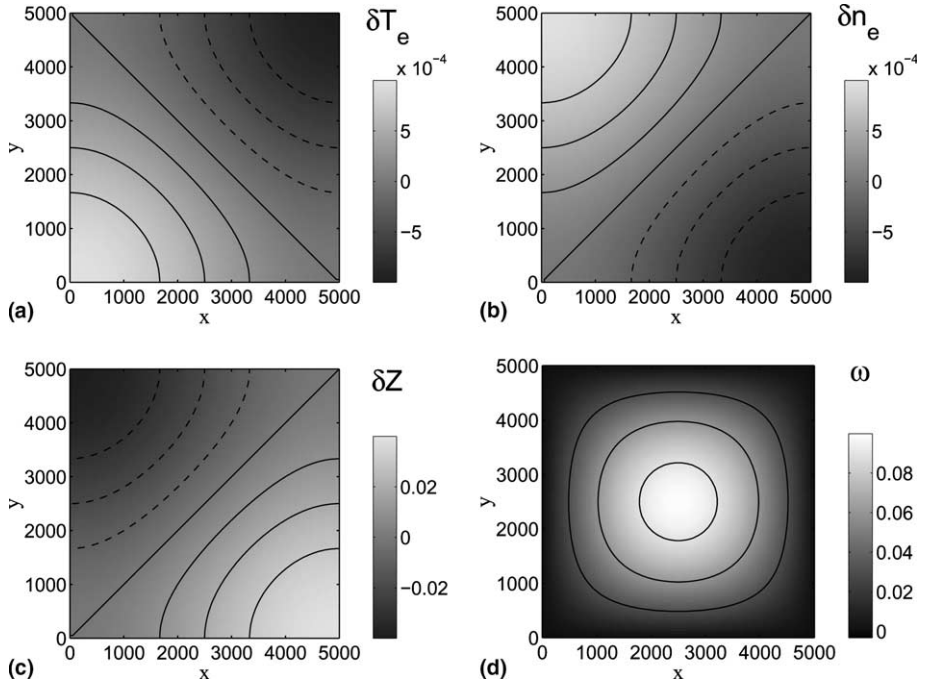

Fig. 3. Profiles for classical transport test. (a) δT_e, (b) δn_e, (c) δZ and (d) magnetic field profile. Dashed contours denote negative iso-value. All quantities are in normalised units given in Eq. (12).

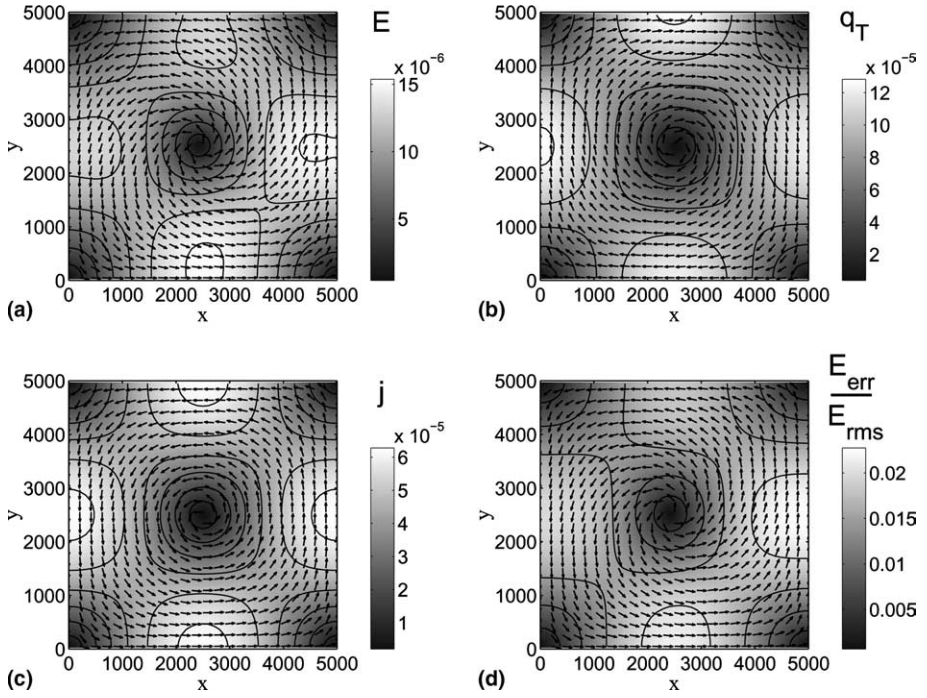

Fig. 4. Profiles of (a) electric field, (b) total heat flow, (c) electric current, and (d) error in the E-field from IMPACT at the x-cell boundaries at $t = \Delta t = 0.5$. The E-field error shown is defined as $(E_j|_{\text{code}} - E_j|_{\text{an.}})/\langle|\mathbf{E}|_{\text{an.}}\rangle_{\text{rms}}$. Contours represent the magnitude of the field while arrows denote its direction. Contours are plotted in steps of 2.5×10^{-6}, 2.5×10^{-5}, 10^{-5}, and 5×10^{-3} for $\mathbf{E}$, $\mathbf{q}_{\text{T}}$, $\mathbf{j}$, and $\mathbf{E}_{err}$, respectively.

itself is accurately obtained by virtue of the current contraint; j_x^X and j_y^X are correct to 0.12% and 0.018%, respectively. These errors solely arise from the FD approximation to the curl operator (see Sections 3.3.2 and 3.6) which is why $j_y^X \propto -(\partial_x \omega)^X$ (a 2 point difference) is more accurate than $j_x^X \propto (\partial_y \omega)^X$ (a 4 point difference). In a similar way j_x^Y is more accurate than j_y^Y. IMPACT gets the values of E_x^X and E_y^X correct to within 1.5% while the error in q_x^X and q_y^X is 0.4% and 0.3%, respectively, for this test case. The accuracy of $\mathbf{E}$ and $\mathbf{q}_{\text{T}}$ at the y-cell boundary is virtually identical (but not precisely the same since the system is not 90° rotationally invariant). As well as demonstrating that IMPACT can accurately recover classical transport the results also show the ability of the code to resolve small perturbations. The quoted error values are root-mean-square (rms) differences between the code and analytical values as a percentage of the rms analytical values (calculated using Eq. (57) and (58)), e.g., error $= \langle \mathrm{E_x}|_{\text{code}} - \mathrm{E_x}|_{\text{an.}}\rangle / \langle \mathrm{E_x}|_{\text{an.}}\rangle$, where $\langle \cdots \rangle$ denotes rms averaging over all the $(nx + 1) \times ny$ x-cell boundaries in the domain. All the errors vary smoothly over the domain and almost vanish in places, so that the maximum error anywhere never exceeds about twice the rms error. In order to reveal such good agreement, the analytical values themselves have to be carefully calculated. We numerically calculate the transport coefficients (in the Lorentz limit) using the formulae of Epperlein and Haines [46,47] rather than using 'standard' polynomial fits for $\alpha_\perp$, $\beta_\perp$, etc., which can be over 10% out at the magnetic-field strength present in this test.

We have also investigated how IMPACT converges to the classical result as Δv and Δx are varied. Fig. 5 shows how the E-field and heat flow components from IMPACT converge to the classical values as the velocity resolution is increased at fixed spatial resolution ($nx = ny = 24$). E_x and E_y converge as Δv until high resolution is reached when E_x starts converging quicker. Scaling of the error with Δv is consistent with the use of forward differencing in the $\mathbf{E}\partial_v f_0$ term in the $\mathbf{f}_1$ equation. q_x and q_y converge more slowly than Δv

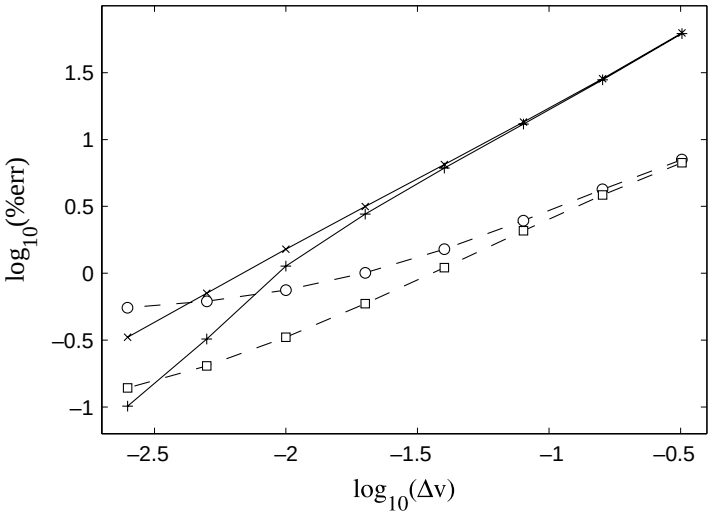

Fig. 5. Convergence of E_x^X, E_y^X, q_x^X and q_y^X (+, ×, ○, and □ symbols, respectively) calculated by IMPACT to the classical transport values as Δv is reduced. The errors shown are root-mean-square (rms) differences between the code and analytical values as a percentage of the rms analytical values, e.g., error $= \langle \mathrm{E_x}|_{\mathrm{code}} - \mathrm{E_x}|_{\mathrm{an.}} \rangle / \langle \mathrm{E_x}|_{\mathrm{an.}} \rangle$ where $\langle \cdots \rangle$ denotes rms averaging over all the $(nx+1) \times ny$ x-cell boundaries in the domain. The code values are calculated using $nx = ny = 24$ and $v_{\max} = 8$.

and the final errors appear to tend to about 0.5% and 0.1% at this spatial resolution. Fig. 6 shows how the errors vary with $1/nx \propto \Delta x$ (with $\Delta x = \Delta y$) when $\Delta v = 0.01$. The errors initially scale as Δx^2 which is consistent with spatial differencing used in the $\mathbf{f}_1$ equations which is centred and therefore second-order accurate in Δs when the x and y cell widths are uniform. The errors in E_x and E_y show evidence of minimizing at around $nx = ny = 10$, which suggests that the overall error in $\mathbf{E}$ is in fact a function of Δv and Δx,

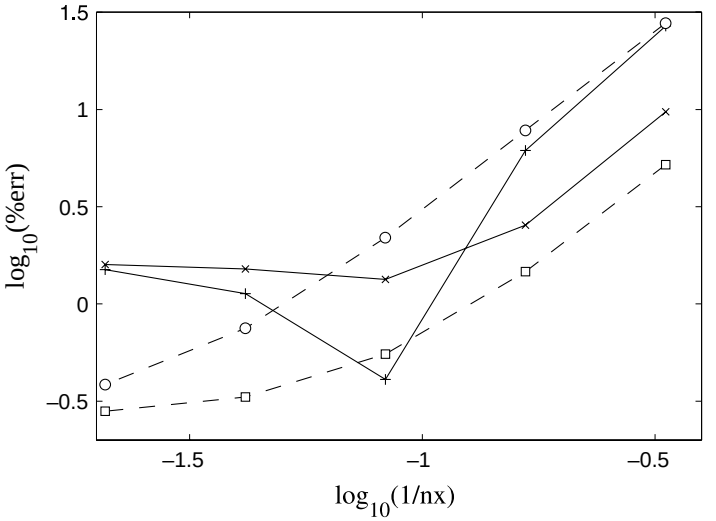

Fig. 6. Convergence of E_x^X, E_y^X, q_x^X and q_y^X (+, ×, ○, and □ symbols, respectively) calculated by IMPACT to the classical transport values as Δx is reduced when $\Delta v = 0.01$. Definition of the percentage error is given in Fig. 5.

Δy. For the system considered here Fig. 6 demonstrates that decreasing Δx below $\sim x_l/10$ without also decreasing Δv is detrimental to the accuracy of E_x and E_y. It should be noted that the local truncation-error function depends on the local shape of the T_e, n_e, Z and ω profiles. Therefore, the optimal way in which to decrease Δv and Δx so as to give the best overall error reduction for all quantities at all places would be difficult, in general.

The dependence of the error on Δx can be removed by calculating the classical values of $\mathbf{E}$ and $\mathbf{q}$ using finite difference approximations for the derivatives ∇T_e, ∇P_e and $\mathbf{j} = \nabla \times \boldsymbol{\omega}$ in Ohm's law and the heat flow equations. As well as handling derivatives in the same way that IMPACT does, i.e., using (35), the transport coefficients are calculated using values of ω, T_e, n_e and $Z^2 n_i$ that have been linearly interpolated from cell-centres to cell-boundaries (as the code does). When using *centred* velocity differencing for $\mathbf{E}\partial_v f_0$ and removing the spatial discretisation error we find that the remaining numerical error scales exactly as Δv^2 as can be seen in Fig. 7(a). Additionally, all quantities have very similar errors. This should be compared to Fig. 7(b) where the spatial discretisation error has not been removed. Note that removal of the spatial discretisation error when using forward velocity differencing results in the numerical error scaling exactly as Δv.

4.2. $\nabla n_e \times \nabla T_e$ B-field generation

There is a well-known mechanism [3,4] that can spontaneously generate magnetic fields in plasma from non-collinear temperature and density gradients; $\partial_t \omega = -(\nabla n_e \times \nabla T_e)/n_e$. It is important to test IMPACT's ability to model B-field generation as this effect was not accessible to previous VFP codes.

The system for testing $\nabla n_e \times \nabla T_e$ magnetic field generation has the following parameters: a size of $x_l \times y_l = 500 \times 500$, a spatial cell size of $\Delta x = \Delta y = 20$, a velocity resolution of (a) $\Delta v = 0.1$ or (b) $\Delta v = 0.02$ (with $v_{\max} = 8$ in both cases), $\delta_c = 10^{-3}$ to keep B-field diffusion to a minimum, and $\Delta t = 5.0$. $Z_0 = 0.1$ is used to boost e–e collisions so that f_0 does not deviate too far from Maxwellian as transport occurs. This keeps IMPACT in the 'local' regime so that meaningful comparison can be made against $\nabla n_e \times \nabla T_e$ B-field generation which is a 'local' mechanism that assumes $f_0 = f_M$. The system is initialised with $\omega = 0$, $\delta T_e = 0.01 \cos(k_x x)$ and $\delta n_e = \delta n_i = 0.01 \cos(k_y y)$, where $k_x = \pi/x_l$ and $k_y = \pi/y_l$. Reflective boundary conditions with $\omega = 0$ and forward velocity differencing for the $\mathbf{E}\partial_v f_0$ term are used. We find that $\nabla n_e \times \nabla T_e$ B-field generation does indeed occur and the resulting magnetic field at $t = 2500$ is shown in Fig. 8(a). The profile of this field has a $\sin(k_x x)\sin(k_y y)$ shape which is in agreement with the prediction of the $\nabla n_e \times \nabla T_e$ mechanism for the temperature and density gradients present. The electric field, total heat flow and electric current at time $t = 2500$ are shown in Figs. 8(b)–(d). The peak growth rate obtained in the simulations compares well with the analytical result as can be seen in Fig. 9. The code gets the initial growth rate to within about 8% and 1% for the $\Delta v = 0.1$ and $\Delta v = 0.02$ runs, respectively, at the start. The subsequent gradual decrease in the growth rate is due to the decay of the temperature perturbation that drives that B-field source. The density perturbation on the other hand is found to remain fixed which is in agreement with the expected behaviour of the numerical scheme.

4.3. B-field resistive diffusion and Ohmic heating

Resistive diffusion of the magnetic field and Ohmic heating of the plasma by currents are related phenomena. The dissipative losses that cause the B-field to diffuse transfer energy from the magnetic field to the thermal energy of the plasma so that (in the absence of the displacement current), the total energy $W_T = \int (U_e + \omega^2/2\delta_c^2)\,\mathrm{d}^3x$ in a closed system does not change. The equations for resistive diffusion of magnetic field and Ohmic heating are (in normalised form) $\dot{\boldsymbol{\omega}} = -\delta_c^2 \nabla \times (\alpha_\perp \nabla \times \boldsymbol{\omega})$ and $\dot{U}_e|_{\mathrm{Ohm}} = \mathbf{E} \cdot \mathbf{j} = \alpha_\perp j^2 = \alpha_\perp \delta_c^4 |\nabla \times \boldsymbol{\omega}|^2$.

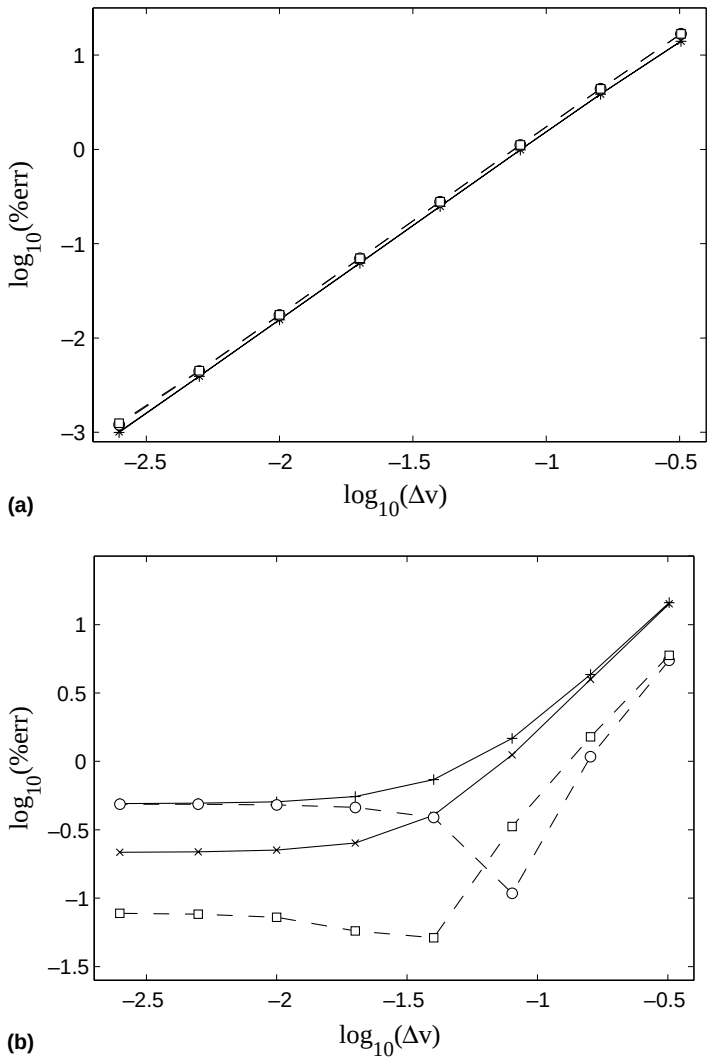

Fig. 7. Reduction of % error in fields calculated by IMPACT with Δv when *central differencing* (rather than forward differencing) is used for the $\mathbf{E}\partial_v f_0$ term. (a) With and (b) without removal of the error contribution from spatial discretisation (see text for detail on how removal is achieved). The code values are calculated using $nx = ny = 24$ and $v_{\max} = 8$. See Fig. 5 for meaning of symbols.

We use the following setup to test the code on these effects: $x_l = 600$ and $\Delta x = 20$ (a 1-D system) $v_{\max} = 8$, $\delta_c = 5$ to promote diffusion and heating, $Z_0 = 10$, and $\Delta t = 0.5$. The initial magnetic field profile is $\omega(x) = 0.1\sin(k_x x)$ with $k_x = \pi/x_l$ while the temperature and density profiles are uniform at $t = 0$. Under these conditions the magnetic field initially accounts for about 8% of the total energy. Reflective boundary conditions with $\omega = 0$ at the edges are employed and the Rosenbluth coefficients are recalculated for each nonlinear iteration. Fig. 10 shows how the magnetic-field energy (solid line, without symbols) decreases with time. Total energy is not quite conserved but gradually decreases with time as shown. For $\Delta v = 0.1$, the Ohmic heating is about 9% lower than it should be which is why energy is being lost from the system. Increasing the velocity resolution results in a linear reduction of the Ohmic heating error with Δv as can clearly be seen by the downwards vertical shift of the 'total energy loss' curves. This is consistent with the

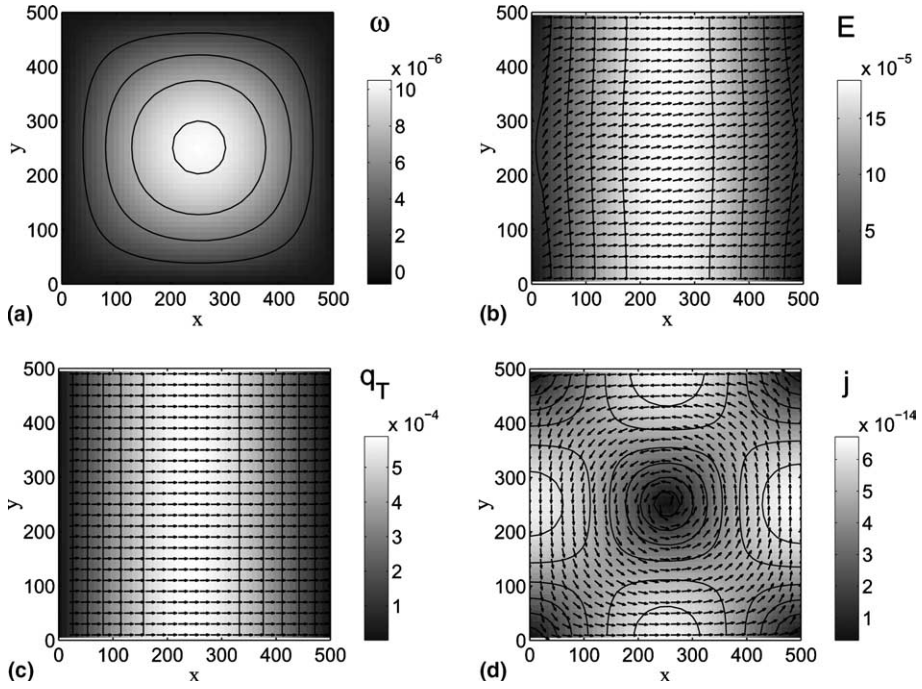

Fig. 8. (a) $\nabla n_e \times \nabla T_e$ generated magnetic field at $t = 2500$. The corresponding electric field, total heat flow vector and electric current are shown in (b), (c), and (d), respectively. Contours are displayed in steps of 2.5×10^{-6}, 4×10^{-5}, 10^{-4}, and 10^{-14} in (a) to (d), respectively. All quantities are in normalised units given in Eq. (12).

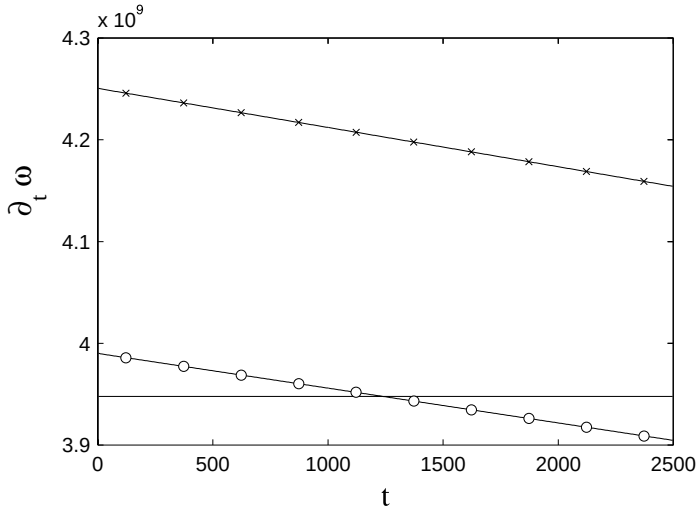

Fig. 9. Comparison of the peak $\nabla n_e \times \nabla T_e$ B-field growth rate $\partial_t \omega$ as calculated by IMPACT using $\Delta v = 0.1$ and $\Delta v = 0.02$ ($\times$ and $\bigcirc$, respectively) with the analytical, classical growth rate (solid curve). Decay of the temperature gradient due to thermal conduction is not taken into account in the analytical value of $\dot{\omega}$.

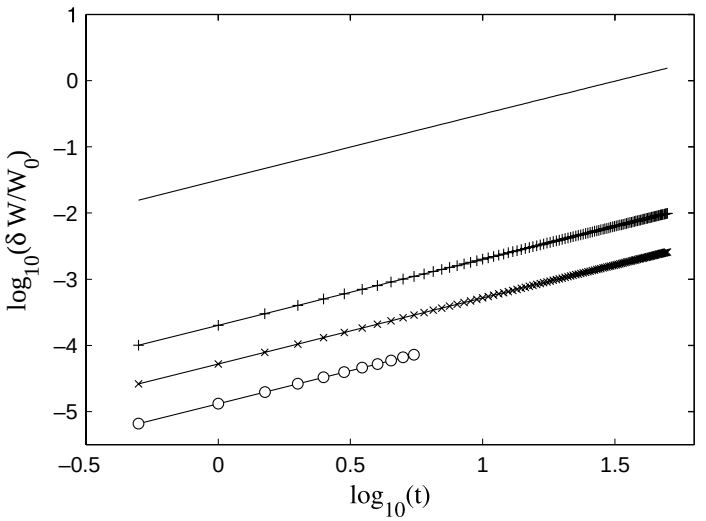

Fig. 10. Percentage *reduction* in magnetic energy, i.e., $W_B|_{t=0} - W_B(t)$, due to resistive diffusion (black curve) and percentage *decrease* in total energy, i.e., $W_T|_{t=0} - W_T(t)$, for $\Delta v = 1/10, 1/40, 1/160$ (+, ×, and ○, respectively).

forward velocity differencing used in the $\mathbf{E} \cdot \partial_v(v^2\mathbf{f}_1)$ term in the f_0 equation. The accuracy of Ohmic heating is found to be similar in 2-D.

To test magnetic-field diffusion in 2-D we use a reduced initial B-field amplitude of $\omega_0 = 10^{-3}$, but keep the same domain size and mesh sizes; $\Delta x = \Delta y = 20$, $\Delta v = 0.1$. Though B-field diffusion occurs in the Ohmic heating test system above where $\omega_0 = 0.1$, it is nonlinear because the diffusion coefficient $\delta_c^2\alpha_\perp$ depends on ω and varies significantly with position and time for this larger magnetisation. The B-field diffusion equation would itself have to be solved numerically in order to obtain an accurate benchmark to compare IMPACT against. Instead we opt for $\omega_0 = 10^{-3}$ which makes the diffusion linear allowing the benchmark result to be readily obtained; $\omega(t) = \omega(t=0)\exp(-t/\tau_c)$, where $\tau_c = [(k_x^2 + k_y^2)\delta_c^2\alpha_\perp]^{-1}$ and the resistivity equals the unmagnetised value of $\alpha_0 = \sqrt{\pi}/8$ to within 0.004%. The decay of the B-field is followed for about 2e-foldings. As shown in Fig. 11 the B-field decay from IMPACT (dashed line) is almost the same as the analytical result (solid line) when centred differencing of the $\mathbf{E}\partial_v f_0$ term is used. In this case, the code value for the decay time τ_c is 1.7% larger than the analytical value of 2532.8 . With forward differencing (dotted-dashed line) the decay occurs more quickly than the ideal result and τ_c is about 15% smaller than the analytical value. This larger error in τ_c occurs because $\alpha_\perp$ is not obtained as accurately. In both cases $\Delta t = 5$, $Z_0 = 1$, and $\delta_c^2 = 20$ are used and the Rosenbluth coefficients are updated for each inner/nonlinear iteration. The Ohmic heating error for these runs is again about 8% and not quite all of the magnetic field energy is transferred to the plasma as the field decays.

4.4. $\nabla T_e \times \nabla(\nabla^2 T_e)$ non-local B-field generation

The tests so far have proved that IMPACT correctly recovers classical transport phenomena. We now introduce a test to verify the code beyond the classical, fluid limit. This test checks whether the code can correctly model magnetic field generation from a non-uniform temperature profile when $\nabla n_e = 0$. This is a non-local effect that arises when f_0 is allowed to become non-Maxwellian [8]. Under these conditions the $\nabla n_e \times \nabla T_e$ mechanism, which is based on classical transport and therefore uses the local approximation, predicts that no magnetic field would be produced. The equation for the early stages of non-local B-field generation (in normalised form) is

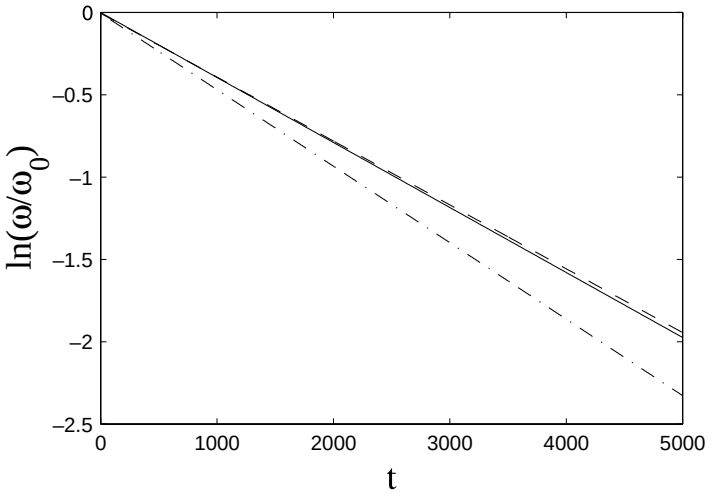

Fig. 11. Comparison of exponential B-field decay. The analytical value of $\omega(t)/\omega_0$ (solid curve) is shown alongside the code results for forward (dotted–dashed curve) and centred (dashed curve) differencing of the $\mathbf{E}\partial_v f_0$ term.

$$\dot{\boldsymbol{\omega}}_{\mathrm{NL}} = -154.21\frac{T_{\mathrm{e}}^{3/2}}{Z^2 n_{\mathrm{i}}}[\nabla T_{\mathrm{e}} \times \nabla(\nabla^2 T_{\mathrm{e}})] \tag{59}$$

assuming that $f_0|_{t=0} = f_{\mathrm{M}}$ (at each spatial point), $\omega|_{t=0} = 0$, and that the temperature perturbation is small, i.e., $\delta T(\mathbf{r}) < T_0$, where $T_{\mathrm{e}} = T_0 + \delta T(\mathbf{r})$. Eq. (59) is valid so long as decay of the temperature profile is negligible and f_0 does not deviate far from Maxwellian. e–e collisions and $\partial_t \mathbf{f}_1$ are ignored when deriving (59) from the VFP equations (13) and (14). (Note the sign of Eq. (1) in [8] is wrong and should be −ve as in (59) here.) This non-local B-field generation mechanism is a higher order effect than the $\nabla n_{\mathrm{e}} \times \nabla T_{\mathrm{e}}$ source and is therefore a more stringent test of the code. Also this effect tests that the numerical implementations of both the f_0 and $\mathbf{f}_1$ equations couple together in the correct way. Additionally, testing the code against the non-local mechanism determines whether the numerical implementation of the $\mathbf{f}_1$ equation and Ampère's law work correctly when $f_0 \neq f_{\mathrm{M}}$ (unlike the previous tests).

To perform the test, we use a large system of size $x_l \times y_l = 3000 \times 1000$, $nx = 180$, $ny = 60$, $\Delta v = 1/20$ and $v_{\max} = 7$. The initial temperature perturbation is plotted in Fig. 12(a) and is described by the equation $\delta T = 0.0025[1 - \tanh\{(x - x_0(y))/d\}]$ with $x_0(y) = (x_l/2) + (y_l/8)\cos(\pi y/y_l)$ and $d = x_l/6$, while $T_0 = 0.5$ (which corresponds to $v_t = 1$ with our normalisations) and $\omega|_{t=0} = 0$. Other parameters used are $\delta_{\mathrm{c}} = 10^{-3/2}$ and $\Delta t = 5$. Central differencing was used in the $\mathbf{E}\partial_v f_0$ term. The non-local B-field from IMPACT at $t = \Delta t$ depicted in Fig. 12(b) is larger than the analytical result shown in Fig. 13(a) and there are differences between the two profiles. The reason for this discrepancy is that the non-local mechanism is not yet fully resolved numerically and smaller values of Δv and Δx, Δy are needed. It turns out that the numerical algorithm yields $\nabla \times \mathbf{E} \neq 0$ at $t = 0$ (shown in Fig. 14) even though $f_0 = f_{\mathrm{M}}$ at this time so that $\mathbf{E} = -\nabla T_{\mathrm{e}}$ and $\dot{\boldsymbol{\omega}} = -\nabla \times \mathbf{E} = 0$ should ideally be the case initially. Just considering the effect of velocity discretisation alone, the way the scheme calculates $\mathbf{E}$ actually yields $\mathbf{E} = -\{\nabla\{n_{\mathrm{e}} T_{\mathrm{e}}^{5/2} + \mathrm{O}(\Delta v)\}\}/\{n_{\mathrm{e}} T_{\mathrm{e}}^{3/2} + \mathrm{O}(\Delta v)\}$ (when $\omega = 0$ and $f_0 = f_{\mathrm{M}}$). In general, elimination of the error terms $\mathrm{O}(\Delta v)$ would still not ensure $\nabla \times \mathbf{E} = 0$ precisely because spatial discretisation means that the identity $\nabla \times \{(\nabla g^a)/g^b\} = 0$ does not quite hold numerically for an arbitrary 2-D profile g even for uniform grids. Subtracting this 'systematic' numerical error from the raw code result yields a corrected B-field (Fig. 13(b)) that agrees well with the analytical result. The correction used is $\boldsymbol{\omega}_{\mathrm{corr}}|_{t=\Delta t} = \boldsymbol{\omega}_{\mathrm{raw}}|_{t=\Delta t} + \Delta t(\nabla \times \mathbf{E}|_{t=0})$. Comparison of the figures shows that

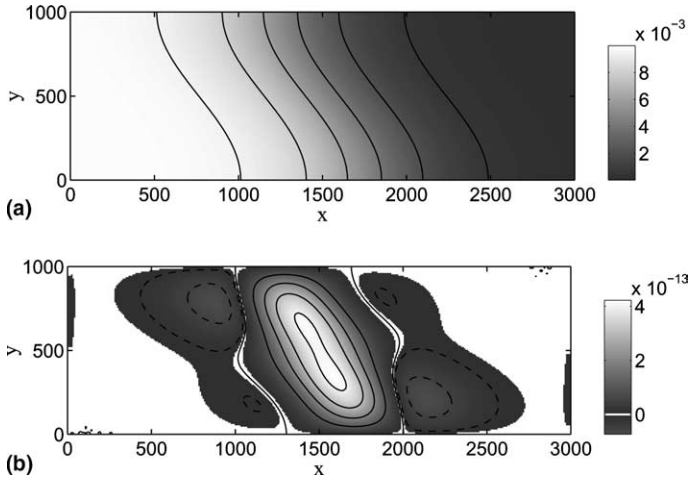

Fig. 12. (a) Initial, non-uniform temperature perturbation causing B-field growth even though $\nabla n_e = 0$. (b) Non-local magnetic field profile at Δt.

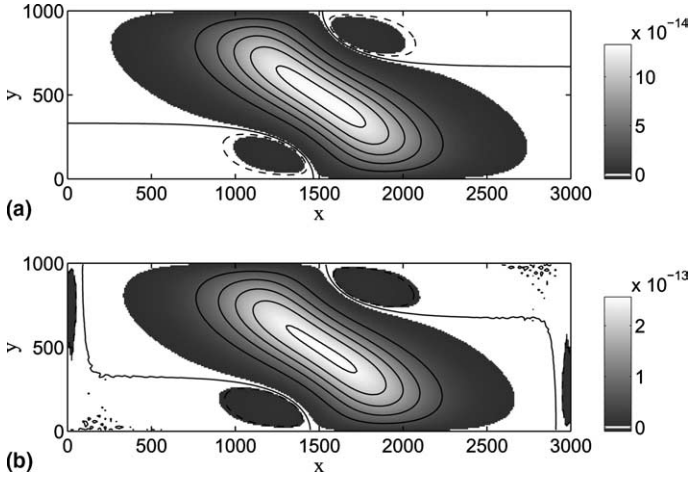

Fig. 13. (a) Analytical value for non-local magnetic field due to the $-\nabla T_e \times \nabla(\nabla^2 T_e)$ mechanism. (b) Corrected, non-local magnetic field profile at Δt from code.

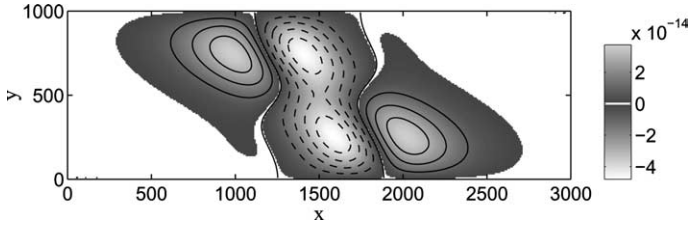

Fig. 14. Finite differencing error in $\nabla \times \mathbf{E}$ at $t = 0$. Analytically, $\nabla \times \mathbf{E} = 0$ initially since $\mathbf{E} = -\nabla T_e$ at $t = 0$.

the profile/shape of the corrected, numerical, *B*-field almost exactly agrees with the solution of Eq. (59) but the magnitude is overestimated by a factor of 2. The reason why the numerical value is twice the analytical value stems from the backwards time differencing used in Faraday's law (51). The non-local mechanism makes $\nabla \times \mathbf{E}$ increase linearly with time from zero. Hence using $(\nabla \times \mathbf{E})^{n+1}$ results in twice the correct value after the first time step. The backwards time differencing result ω_{BT} converges to the exact value $\omega_{\mathrm{ex.}}$ as $\omega_{\mathrm{BT}}/\omega_{\mathrm{ex.}} = (n+1)/n$ with increasing time (ignoring errors due to spatial discretisation). Centred time differencing of Faraday's law would alleviate this temporal discretisation error. We note that repeating this test with better numerical resolution should see the systematic, numerical $\nabla \times \mathbf{E}|_{t=0} \neq 0$ error reduce to a level that is negligible compared to the real physical effect. Then correction of the raw result would be unnecessary. Alternatively, keeping the resolution used here but making the comparison at a later time when (i) the physical effect ($\propto t^2$) dominates over the numerical error ($\propto t$) but (ii) Eq. (59) is still valid would see better agreement between the raw numerical and exact results.

4.5. Other tests

IMPACT is able to accurately follow the exponential decay of an initial, long wavelength, temperature perturbation $\delta T_{\mathrm{e}}/T_0 = 0.01\cos(k_x x)$ when $\omega_0 = 0.1$, $x_l = 3000$, using a *very large* time step of $\Delta t = 2000$. (Other parameters are $nx = 20$, $\Delta v = 0.025$, $v_{\max} = 6$ and $Z = 10$.) This time step is still smaller than the characteristic decay time of $\tau_c \sim 9.3 \times 10^4$ though. The decay constant obtained from the code is accurate to within 1% over the duration of the run and the mass and thermal energy in the system are conserved to better than $0.3 \times 10^{-9}\%$ and $6 \times 10^{-9}\%$, respectively, at $t = t_{\max} = 2 \times 10^5$. Initially about 2000 nonlinear iterations (per time step) are needed for the solution to converge. This drops to about 1500 at the end of the run. The excellent energy conservation of $6 \times 10^{-9}\%$, possible because Ohmic heating is turned off, verifies that Langdon's method for making the Fokker–Planck *e–e* collision operator conserve energy works. The number of nonlinear iterations per time step can be reduced if less stringent energy conservation is required. Note that the Rosenbluth coefficients must be updated within the nonlinear iteration for this test. The effect of *e–e* collisions on f_0 is not properly estimated for large Δt when the Rosenbluth coefficients are treated explicitly which manifests itself through gross inaccuracies in transport (e.g., apparent suppression of thermal conductivity) as well as a loss of energy conservation.

The interplay between the number of nonlinear iterations per time step and Δt for systems with $L_T, L_n \gg \overline{\lambda}$, where things evolve slowly compared to $\overline{\tau}$, has been investigated using a test problem similar to the one above. The only differences are that Ohmic heating is included, $\Delta v = 0.1$, and the matrix solver and nonlinear iteration tolerances are relaxed from $\sim 10^{-11}$ and 10^{-15} to 10^{-10} and 10^{-9}. Both $Z = 1$ and 10 have been tried. When Δt exceeds the order of 1 to $10\tau_{\mathrm{ee}}$ and the Rosenbluth coefficients are updated within the nonlinear iteration, a further increase in Δt is accompanied by an almost equal increase in the number of nonlinear iterations required, resulting in a marginal saving in computational effort overall. For example, when $Z = 10$, with $\Delta t = 50$ it takes 220 s, a total of 797 nonlinear iterations, and a total of 33,920 matrix solver iterations to reach $t = 2000$ (totals are accumulated over each time step) while using $\Delta t = 2000$ takes 190 s, 596 nonlinear iterations, and 53,959 matrix solver iterations to reach the same time. (See the caption for Table 1 for a description of the hardware used.) In this case, using $\Delta t = 2000$ proves to be quicker because building the matrix is much more 'expensive' than solving the matrix equation. Nevertheless, it is preferable to limit the time step to around $5\tau_{\mathrm{ee}}$ so that a more accurate solution can be attained for only marginally more computational effort. The number of nonlinear iterations is unlikely to change much if a finer grid is used, or even if the system were 2-D (as long as τ_c remains similar), but the relative cost of calculating matrix coefficients compared to solving the matrix decreases. This suggests that for expansive systems (i.e., $L_T, L_n \gg \overline{\lambda}$) with a large number of grid points in phase space, very large time steps may not minimize the computational effort. In comparison, for smaller scale systems where non-local effects are

Table 1
CPU time, memory usage, and average number of nonlinear iterations per time step for a selection of the test runs

Section	4.1	4.2	4.3	4.4	4.5
Figure	5 and 6	9	11	12 and 13	–
nv, nx, ny	800, 24, 24	400, 25, 25	80, 30, 20	140, 180, 60	240, 40, 1
nt	1	500	1000	1	100
Δt	0.1	5	5	5	2000
Matrix solver tolerance	10^{-15}	10^{-13}	10^{-13}	10^{-13}	$\sim 10^{-11}$
Nonlinear iteration tolerance	10^{-13}	10^{-11}	10^{-11}	10^{-12}	10^{-15}
RB coefficient iterated?	Yes	No	Yes	No *e–e* collision	Yes
nd	482,000	262,000	52,100	1,560,000	10,100
N_{sparse}	19,300,000	10,500,000	2,020,000	61,600,000	244,000
Average nonlinear iterations	3	2	15.7	3	1732
Total CPU time	2.5 min	57 h	24 h	15 min	138 h
Memory usage	580 MB	293 MB	62 MB	1.8 GB	15 MB

These tests were run on a single 2 GHz Pentium 4 Xeon processor of a 'DELL Precision 530' workstation with 2 GB of RAM running Linux. Programs were compiled using the Gnu Fortran 77 compiler. A summary of important run parameters are included. The dimension of the matrix nd and the number of non-zero elements N_{sparse} are listed to three significant figures. Convergence of the matrix solver is achieved when $\|A \cdot x - B\|_2 / \|B\|_2 < \text{TOL}$, while nonlinear iteration convergence is achieved when the fractional change in $\|x\|_2$ drops below the desired tolerance.

prominent, the time step will need to be small enough to resolve the phenomena of interest and very large time steps are not appropriate.

We have also tested the *e–e* collisions in IMPACT by following the collisional relaxation of f_0 to f_M when initially non-Maxwellian [48]. The results obtained originally in [48] and later refined in [49] were recovered.

Finally, a similar set up to that used by Kho and Haines [17] to address convection of magnetic field by heat flowing from the critical surface to the ablation surface has been tried. We find qualitative agreement, also seeing amplification of the magnetic field injected at the low density edge of the density ramp (where heating is applied) as it is subsequently convected with the heatflow up the density ramp.

4.6. Run times and memory usage

A list of CPU time, memory usage and the average number of nonlinear iterations required per time step, for representative runs from each test is given in Table 1. Pertinent run parameters such as the time step, the number of grid cells in each dimension, convergence tolerances, and whether the Rosenbluth coefficients are treated explicitly or lagged in the nonlinear iteration, are also given there. A description of the hardware and convergence tests can be found in the table caption. An important point to note is that all the tests reported in Table 1 were run using IMPACT's fast but memory inefficient mode. In this mode, each matrix element effectively appears twice in memory. Initially they are stored in auxiliary arrays corresponding to G, H, M, and N in Eqs. (52) and (53) as they are calculated. They are then packed into compressed row format which permits fast matrix multiplication. This later optimisation can be omitted, lowering the memory overhead by nearly half, but then the matrix row and column indices of each element have to be recalculated 'on the fly' every time a matrix multiplication operation is required.

5. Discussion

The test results in the previous section show that IMPACT can reproduce classical, transport phenomena. The $\nabla T_e \times \nabla(\nabla^2 T_e)$ non-local B-field generation test shows that it also works correctly beyond the

classical limit and can resolve very small perturbations with good accuracy. At present PIC codes with collisions would not be able to show this effect being unable to enter a sufficiently collisional regime and being too noisy to resolve the perturbation of the distribution function well enough. Hybrid transport codes cannot describe this type of non-local B-field generation either because they treat the background medium non-kinetically. The simulation results presented in [8] show that the code in fact works far beyond the classical limit; it works in a highly non-local, nonlinear regime where f_0 becomes strongly distorted by powerful, localized laser heating. The results of the B-field diffusion and temperature-perturbation decay tests demonstrate that a large time step can be used.

We find that turning on the electron inertia term $\partial_t \mathbf{f}_1$ makes the iterative Bi-CGSTAB (or Bi-CG) matrix solver converge to the solution in less iterations therefore increasing the overall speed of the code. For instance, in the case of the B-field diffusion test-problem inclusion of electron inertia reduces the total number of matrix solver iterations per time step (summed over the $\sim$22 nonlinear iterations) from $\sim$700 to 600–650. Under the more extreme conditions considered in [8] electron inertia drastically reduces the total number of matrix solver iterations (per time step) by a factor of 24 or more. The reason why electron inertia speeds up the solution of the matrix is that it introduces an advective character into the system. Without it, propagation of disturbances in f_0 across the spatial grid is completely diffusive. Spatial diffusion is *extremely* rapid for the high velocity part of f_0 since the effective diffusion coefficient scales as $D_s \propto v^5$. Introduction of advection helps to reduce the 'connectivity' between distant points on the spatial grid for the high velocity parts of f_0 which in turn reduces the number of matrix solver iterations required. When electron-inertia is turned on we find that the scheme can become unstable if very cold and dense plasmas (i.e., $\delta_c > 1$) and small system sizes (i.e., a few λ_n long) are used.

We find that the algorithm conserves mass exactly as expected and that energy is conserved to $O(\Delta v)$ with the Ohmic heating term in the f_0 equation being the cause of energy non-conservation. Use of the current constraint together with the implicit treatment of $\mathbf{E}$ completely overcomes the problems in maintaining quasineutrality [16] encountered with previous VFP codes. In terms of transport the scheme is $O(\Delta s^2)$ accurate in the spatial cell size and either $O(\Delta v)$ or $O(\Delta v^2)$ accurate in the velocity cell size for centred and forward differencing of the $\mathbf{E}\partial_v f_0$ term in the $\mathbf{f}_1$-equation, respectively. We have shown that in general changing Δv without also changing Δs in the correct way (or vice versa) will not necessarily improve the overall accuracy. The temporal accuracy of the scheme varies with physical effect. The local truncation error for spatial diffusion is $O(\Delta t)$ while introduction of electron inertia results in spatial advection which is $O(\Delta t^2)$ accurate. Magnetic field growth/decay is $O(\Delta t)$ accurate at present. The tests reported here use regular grids in x, y and v. Use of an irregular x-grid, for example, would generally be expected to result in a deterioration of the accuracy of the $O(\Delta x^2)$ parts of the scheme towards $O(\Delta x)$. But the amount of $O(\Delta x)$ error introduced in this case will depend on how abruptly Δx_i varies from cell to cell. For smoothly changing cell size, the extra $O(\Delta x)$ error should be negligible. Another effect of using an irregular spatial grid is that, unless care is taken, it can be shown that $[\nabla \cdot (\nabla \times \mathbf{B})]_{ij} = [\nabla \cdot \mathbf{j}]_{ij} \neq 0$ and therefore exact quasineutrality can be lost.

A key area for future improvement is the Ohmic heating term. This could be made $O(\Delta v^2)$ accurate or differenced to ensure that there is no Ohmic heating when $\mathbf{j} = 0$. Improved preconditioning would reduce the number of Bi-CGSTAB iterations needed to solve the sparse matrix equation. This would bring 2 benefits, namely reduction of the CPU time needed per time step and a decrease in the build up of machine rounding errors. Epperlein's linearisation of the Fokker–Planck collision operator [42] would enable the scheme to converge in fewer nonlinear iterations when using large times steps but would introduce a lot of extra non-zero matrix elements. Inclusion of e–e collisions in the $\mathbf{f}_1$ equation could be achieved at practically no cost if treated explicitly. Implicit treatment would however mean that $\mathbf{f}_1^{n+1}$ cannot be eliminated from the FD equation set and hence require reformulation of the sparse matrix plus increase the number of non-zero matrix elements. Other avenues for improvement are: (1) inclusion of

more B-field components which would require inclusion of E_z and f_z too, and (2) adaptation for 2-D cylindrical r, z geometry.

Though we have neglected the displacement current in this paper, it can easily be added since it does not change the matrix sparsity pattern. Doing so would mean that $\partial_t n_e$ would no longer be identically zero and departures from strict quasineutrality are permissible. This would probably improve IMPACT's ability to deal with very steep density gradients by allowing debye sheaths to form in these regions. We note that the addition of displacement current to IMPACT is in progress. Ideally, ion motion needs to be added since intense laser illumination leads to ion motion near the critical surface (in long density scalelength plasmas) and deformation of the surface of ionized solid-targets (short density scalelength, dense plasmas), both of which affect gross electron dynamics. Addition of hydrodynamics has been considered in 2-D VFP codes without B-fields before [16]. It should be possible to include them in IMPACT too. Ionisation dynamics could be important depending on the details of the system. For an intense laser pulse interacting with an initially unionized, thick (100's of μm thick), high Z foil target, field ionisation by the laser would be extremely rapid at the surface but collisional ionisation within the depths of the target would follow (and affect) the penetration of a heat front through the target. Because transport coefficients depend strongly on the ionisation state, ionisation dynamics would be important here. Conversely, for a thin target or a low Z plasma, the plasma would quickly be fully ionized throughout and ionisation dynamics would be unimportant. Ionisation dynamics (including recombination) have previously been added to 1-D VFP codes [50] and could in principle be added to a code like IMPACT.

It should be remembered that IMPACT uses the diffusion approximation whereby $\mathbf{f}_2$ and higher orders terms in the expansion of the electron distribution are neglected. The effect of $\mathbf{f}_2$ (and higher orders) on the tests presented here would be negligible since the components of the Cartesian tensor series are ordered as $f_0 \sim \epsilon^{-1} f_1 \sim \epsilon^{-2} f_2$, etc., where $\epsilon = \lambda_n / L$, and $\lambda_n \ll L$ throughout. Investigation of the effect of $\mathbf{f}_2$ on transport when B-fields are present and the scalelengths L_n, L_T become similar to the mean-free-path (so that the ordering $f_0 > |\mathbf{f}_1| > |\mathbf{f}_2| > \cdots$ breaks down) requires inclusion of $\mathbf{f}_2$ into IMPACT. We note that inclusion of $\mathbf{f}_2$ (and higher orders) was previously shown not to substantially affect heat flow down steep temperature gradients in an unmagnetised plasma [14]. We expect this still to hold in the magnetised case when L_B the magnetic field scale length is large compared to $\overline{\lambda}$. On the other hand, strong, short scale length magnetic variations perpendicular to a steep temperature gradient would tend to laterally separate the hotter electrons travelling down the temperature gradient from the colder electrons flowing up thus forming filaments. Once this occurs we anticipate that a proper description of energy transport would require the higher order terms neglected in the diffusion approximation.

Addition of $\mathbf{f}_2$ and even higher orders, together with displacement current would extend the code's range of applicability into the collisionless regime. When doing this relativistic effects would need to be included too, but would actually be beneficial since it would restrict the speed of electron propagation to below the speed of light. We note that we are in the process of developing a complementary 2-D VFP code [51], designed to a tackle a different regime than IMPACT, that goes a lot of the way towards these aims: an arbitrary number of spherical harmonics can be used in the expansion of f, it is relativistically correct, and includes displacement current. In essence, it will have the capabilities of a Vlasov code but with electron collisions accurately incorporated. It is proving to be adept at dealing with fast electron transport through solid density plasma, and combines favourable aspects of explicit PIC (fully kinetic) and hybrid modelling (collisional background plasma) into one package. In contrast to IMPACT this code is not fully implicit, but rather uses explicit differencing in the spatial directions, which is feasible since relativistic effects are incorporated. It should be pointed out that IMPACT still remains better suited to dealing with thermal transport in the presence of steep temperature and density gradients and magnetic fields, though.

6. Conclusions

In conclusion, we have described the first 2-D Vlasov–Fokker–Planck code to self-consistently include magnetic fields. It is designed to model electron transport in the presence of magnetic fields and magnetic field generation in laser–plasma interactions but may also have application in other areas such as astrophysical modelling. The code, called IMPACT, has the unique capability of being able to describe these phenomena with *all* electrons being treated kinetically and therefore can access regimes/conditions where fluid codes (based on classical, transport theory) and hybrid transport codes are not valid. The code incorporates other innovations in addition to the inclusion of magnetic field. Its unique differencing scheme treats both the electric field and the distribution function implicitly which makes the code robust and able operate with a large time step. It also retains electron inertia which improves the efficiency of the code while increasing the realism of the model at the same time. We have shown that IMPACT can both accurately describe existing, classical, transport phenomena plus describe new phenomena based on non-local effects too. Improvements have been identified which will extend the range of applicability of the code.

Acknowledgements

This work is supported by the U.K. Engineering and Physical Sciences Research Council under Grants No. GR/M38988 and GR/R71979.

References

[1] S.I. Braginskii, Transport processes in a plasma, in: Reviews of Plasma Physics, Consultants Bureau, New York, vol. 1, p. 205.
[2] L. Spitzer Jr., R. Härm, Transport phenomena in a completely ionized gas, Phys. Rev. 89 (1953) 977.
[3] L. Biermann, Uber den Ursprung der Magnetfelder auf Sternen und im interstellaren Raum, Z. Naturf. A 5 (1950) 65.
[4] J.A. Stamper et al., Spontaneous magnetic fields in laser-produced plasmas, Phys. Rev. Lett. 26 (1971) 1012.
[5] M.G. Haines, Magnetic-field generation in laser fusion and hot-electron transport, Can. J. Phys. 64 (1986) 912.
[6] M. Zepf et al., Fast particle generation and energy transport in laser–solid interactions, Phys. Plasmas 8 (2001) 2323;
J.T. Mendonca, J.R. Davies, M. Eloy, Proton and neutron sources using terawatt lasers, Meas. Sci. Technol. 12 (2001) 1801.
[7] M. Tabak et al., Ignition and high gain with ultrapowerful lasers, Phys. Plasmas 1 (1994) 1626;
M.G. Haines, Review of inertial confinement fusion, Astrophys. Space Sci. 256 (1998) 125.
[8] R.J. Kingham, A.R. Bell, Nonlocal magnetic-field generation in plasmas without density gradients, Phys. Rev. Lett. 88 (2002) 045004.
[9] S.H. Glenzer et al., Thomson scattering from laser plasmas, Phys. Plasmas 6 (1999) 2117.
[10] R.M. Kulsrud, R. Cen, J.P. Ostriker, D. Ryu, The protogalactic origin for cosmic magnetic fields, Astrophys. J. 480 (1997) 481;
N.Y. Gnedin, A. Ferrara, E.G. Zweibel, Generation of the primordial magnetic fields during cosmological reionization, Astrophys. J. 539 (2000) 505;
G. Davies, L.M. Widrow, A possible mechanism for generating galactic magnetic fields, Astrophys. J. 540 (2000) 755.
[11] A.R. Bell, J.R. Davies, S. Guérin, H. Ruhl, Fast-electron transport in high-intensity short-pulse laser–solid experiments, Plasma Phys. Control. Fusion 39 (1997) 653.
[12] S.M. Guérin, A.R. Bell, J.R. Davies, M.G. Haines, One-dimensional particle simulations of fast electron transport in solid targets, Plasma Phys. Control. Fusion 41 (1999) 285.
[13] A.R. Bell, R.G. Evans, D.J. Nicholas, Electron energy transport in steep temperature gradients in laser-produced plasmas, Phys. Rev. Lett. 46 (1981) 243.
[14] J.P. Matte, J. Virmont, Electron heat transport down steep temperature gradients, Phys. Rev. Lett. 49 (1982) 1936.
[15] E.M. Epperlein, G.J. Rickard, A.R. Bell, Two-dimensional nonlocal electron transport in laser-produced plasmas, Phys. Rev. Lett. 61 (1988) 2453;
G.J. Rickard, A.R. Bell, E.M. Epperlein, 2D Fokker–Planck simulations of short-pulse laser–plasma interactions, Phys. Rev. Lett. 62 (1989) 2687.

[16] E.M. Epperlein, G.J. Rickard, A.R. Bell, A code for the solution of the Vlasov–Fokker–Planck equation in 1-D or 2-D, Comput. Phys. Commun. 52 (1988) 7;
E.M. Epperlein, Fokker–Planck modeling of electron transport in laser-produced plasmas, Laser Part. Beams 12 (1994) 257.
[17] T.H. Kho, M.G. Haines, Nonlinear kinetic transport of electrons and magnetic field in laser-produced plasmas, Phys. Rev. Lett. 55 (1985) 825;
T.H. Kho, M.G. Haines, Nonlinear electron transport in magnetized laser plasmas, Phys. Fluids 29 (1986) 2665.
[18] R.S. Craxton, M.G. Haines, Hot spots in laser plasmas, Phys. Rev. Lett. 35 (1975) 1336;
R.S. Craxton, M.G. Haines, $\mathbf{J} \times \mathbf{B}$ acceleration of fast ions in laser–target interactions, Plasma Phys. 20 (1978) 487.
[19] D.G. Colombant, N.K. Winsor, Thermal-force terms and self-generated magnetic fields in laser-produced plasmas, Phys. Rev. Lett. 38 (1977) 697.
[20] J.U. Brackbill, S.R. Goldman, Magnetohydrodynamics in laser fusion: fluid modeling of energy transport in laser targets, Comm. Pure Appl. Math. 36 (1983) 415.
[21] J. Dawson, One-dimensional plasma model, Phys. Fluids 5 (1962) 445.
[22] C.K. Birdsall, A.B. Langdon, Plasma Physics Via Computer Simulation, McGraw-Hill, New York, 1985.
[23] C.Z. Cheng, G. Knorr, The integration of the Vlasov equation in configuration space, J. Comput. Phys. 22 (1976) 330.
[24] J.U. Brackbill, D.W. Forslund, An implicit method for electromagnetic plasma simulation in two dimensions, J. Comput. Phys. 46 (1982) 271;
A.B. Langdon, B.L. Cohen, A. Fiedman, Direct implicit large time-step particle simulation of plasmas, J. Comput. Phys. 51 (1983) 107.
[25] M. Honda, J. Meyer-ter-Vehn, A. Pukhov, Two-dimensional particle-in-cell simulation for magnetized transport of ultra-high relativistic currents in plasma, Phys. Plasmas 7 (2000) 1302.
[26] J.M. Wallace et al., Collisional effects on the Weibel instability, Phys. Fluids 30 (1987) 1085.
[27] R.J. Mason, Monte Carlo hybrid modeling of electron transport in laser produced plasmas, Phys. Fluids 23 (1980) 2204.
[28] R.J. Mason, An electromagnetic field algorithm for 2D implicit plasma simulation, J. Comput. Phys. 71 (1987) 429.
[29] J.R. Davies, A.R. Bell, M.G. Haines, S. Guérin, Short-pulse high-intensity laser-generated fast electron transport into thick solid targets, Phys. Rev. E 56 (1997) 7193.
[30] L. Gremillet, G. Bonnaud, F. Amiranoff, Filamented transport of laser-generated relativistic electrons penetrating a solid target, Phys. Plasmas 9 (2002) 941.
[31] R.J. Mason, Double-diffusion hot-electron transport in self-consistent E and B fields, Phys. Rev. Lett 42 (1979) 239;
R.J. Mason, M. Tabak, Magnetic field generation in high-intensity-laser–matter interactions, Phys. Rev. Lett. 80 (1998) 524.
[32] I.P. Shkarofsky, Heat conduction and magnetic field induction in the presence of cold and hot-electron Maxwellian distributions, Phys. Rev. Lett. 42 (1979) 1342.
[33] G.P. Schurtz, Ph.D. Nicolai, M. Busquet, A nonlocal electron conduction model for multidimensional radiation hydrodynamic codes, Phys. Plasmas 7 (2000) 4238.
[34] J.C. Whitney, Finite difference methods for the Fokker–Planck equation, J. Comput. Phys. 6 (1970) 483.
[35] S. Jorna, L. Wood, Fokker–Planck calculations on relaxation of anisotropic velocity distributions in plasmas, Phys. Rev. A 36 (1987) 397.
[36] L. Chacón, D.C. Barnes, D.A. Knoll, G.H. Miley, An implicit energy-conservative 2D Fokker–Planck algorithm, J. Comput. Phys. 157 (2000) 618.
[37] C. Buet, S. Cordier, P. Degond, M. Lemou, Fast algorithms for numerical, conservative, and entropy approximations of the Fokker–Planck–Landau equation, J. Comput. Phys. 133 (1997) 310.
[38] T.W. Johnston, Cartesian tensor scalar product and spherical harmonic expansions in Boltzmann's equation, Phys. Rev. 120 (1960) 1103.
[39] I.P. Shkarofsky, T.W. Johnston, M.P. Bachynski, The Particle Kinetics of Plasmas, Addison-Wesley, Reading, MA, 1966.
[40] A.B. Langdon, Nonlinear inverse Bremsstrahlung and heated-electron distributions, Phys. Rev. Lett. 44 (1980) 575.
[41] J.S. Chang, G. Cooper, A practical difference scheme for Fokker–Planck equations, J. Comput. Phys. 6 (1970) 1.
[42] E.M. Epperlein, Implicit and conservative difference scheme for the Fokker–Planck equation, J. Comput. Phys. 112 (1994) 291.
[43] A.B. Langdon, Conservative differencing of the electron Fokker–Planck transport equation, in: CECAM Report of Workshop on The Flux Limiter and Heat Flow Instabilities in Laser-Fusion Plasmas, Universite Paris Sud, France, 1981, p. 69.
[44] H.A. Van der Vorst, Bi-CGSTAB: a fast and smoothly converging variant of Bi-CG for the solution of nonsymmetric linear systems, SIAM J. Sci. Statist. Comput. 13 (1992) 631.
[45] R. Fletcher, Conjugate gradient methods for indefinite systems, in: G. Watson (Ed.), Proceedings of the Dundee Biennial Conference on Numerical Analysis, Springer-Verlag, New York, 1975.
[46] E.M. Epperlein, M.G. Haines, Plasma transport coefficients in a magnetic field by direct numerical solution of the Fokker–Planck equation, Phys. Fluids 29 (1986) 1029.
[47] E.M. Epperlein, J. Phys. D 17 (1984) 1823.

[48] W.M. MacDonald, M.N. Rosenbluth, W. Chuck, Relaxation of a system of particles with Coulomb interactions, Phys. Rev. 107 (1957) 350.
[49] T.H. Kho, Relaxation of a system of charged particles, Phys. Rev. A 32 (1985) 666.
[50] R.P.J. Town, A.R. Bell, S.J. Rose, Fokker–Planck simulations of short-pulse-laser–solid experiments, Phys. Rev. E 50 (1994) 1413;
R.P.J. Town, A.R. Bell, S.J. Rose, Fokker–Planck calculations with ionization dynamics of short-pulse laser–solid interactions, Phys. Rev. Lett. 74 (1995) 924;
S. Ethier, J.P. Matte, Electron kinetic simulations of solid density Al plasmas produced by intense subpicosecond laser pulses. I. Ionization dynamics in 30 femtosecond pulses, Phys. Plasmas 8 (2001) 1650.
[51] A.R. Bell, R.J. Kingham, Resistive collimation of electron beams in laser-produced plasmas, Phys. Rev. Lett. 91 (2003) 035003.